HIGH-Z METAL ENCAPSULATING CARBON DOTS FOR ENHANCING RADIATION THERAPY

by

CHAEBIN LEE

(Under the Direction of Jin Xie)

ABSTRACT

Cancer is a major health problem worldwide. It is estimated that about 20 % people are diagnosed by cancer, and about 10% people die from cancer. Among the cancer patient, about 50% people receive radiation therapy (RT). Despite of advanced RT techniques, the maximum dose is still limited by the radiation tolerance of surrounding normal tissues. Radiosensitizers are often used along with RT to overcome the dose limitation. With emerging of nanotechnology, high-Z nanoparticles (HZNPs) have attracted attention as a radiosensitizer due to their strong photoelectric effect. Until now, many HZNPs have been proposed, but the most HZNPs nanoparticles are limited to clinical translation due to suboptimal pharmacokinetics, low cellular accumulation, and heavy metal toxicity. Here, high-Z metal loaded carbon dots (M@Cdots) are explored as a novel type of radiosensitizer. The carbon dots (Cdots) are only about 3nm, and they are chemically and biologically inert. Therefore, other than enhanced radiation therapy efficacy, minimal systematic toxicity can be expected.

INDEX WORDS: radiation therapy, high-Z nanoparticles, radiosensitizer, carbon dots

HIGH-Z METAL LOADED CARBON NANOPARTICLE FOR ENHANCED RADIATION THERAPY

by

CHAEBIN LEE

BS, University of Florida, USA, 2013

A Thesis Submitted to the Graduate Faculty of The University of Georgia in Partial
Fulfillment of the Requirements for the Degree

DOCTOR OF PHILOSOPY

ATHENS, GEORGIA

2020

HIGH-Z METAL LOADED CARBON NANOPARTICLE FOR ENHANCED RADIATION THERAPY

by

CHAEBIN LEE

Major Professor:	Jin Xie
Committee:	Sergiy Minko Leidong Mao

Electronic Version Approved:

Ron Walcott
Dean of the Graduate School
The University of Georgia
December 2020

TABLE OF CONTENTS

Page

ACKNOWLEDGEMENTS iv

LIST OF TABLES vii

LIST OF FIGURES viii

CHAPTER

1 INTRODUCTION AND LITERATURE REVIEW: RADIATION THERAPY AND HIGH-Z NANOPARTICLES 1

- 1.1 Introduction to radiation therapy 1
- 1.2 Principal of radiation therapy 2
- 1.3 Radiation therapy with high-Z nanoparticles 5
- 1.4 Chemical and biological effect of high-Z nanoparticles in radiation therapy 7
- 1.5 Current research on high-Z nanoparticles 11
- 1.6 Limitation of conventional HZNPs and overview of the following chapters 14

2 SYNTHESIS AND CHARACTRERIZATION OF HIGH-Z METAL LOADED CARBON NAOPARTICLS 16

- 2.1 Introduction 18
- 2.2 Materials and Methods 21
- 2.3 Results and Discussion 25

2.4 Conclusion 33

3 ULTRASMALL Gd@Cdots AS A RADIOSENSITIZING AGENT FOR NON-SMALL CELL LUNG CANCER..34

4.1 Introduction..36

4.2 Materials and Methods..38

4.3 Results and Discussion 48

4.4 Conclusion 61

4 HIGH-Z METAL LOADED CARBON NAOPARTICLES AND IN VIVO IMAGING..62

3.1 Introduction..64

3.2 Materials and Methods..66

3.3 Results and Discussion 69

3.4 Conclusion 75

5 CONCLUSION AND FUTURE PLAN 76

REFERENCES 78

APPENDICES 106

LIST OF TABLES

Page

Table 4.1: Serum chemistry of mice treated with Gd@GCNs (0.1 mmol Gd/Kg)............75

LIST OF FIGURES

Page

Figure 1.1: Principle of radiation therapy. Direct damage and indirect damage 3

Figure 1.2: Mechanisms of does accumulation enhancement and secondary electron production by high-Z nanoparticles 7

Figure 1.3: Scheme of impact of HZNPs to the cell. 10

Figure 2.1: Scheme of hydrothermal reaction for M@Cdots synthesis............................25

Figure 2.2: Physiochemical characteristics of Gd@Cdots 27

Figure 2.3: Physiochemical characteristics of Bi@Cdots...28

Figure 2.4: Stability of M@Cdots...30

Figure 2.5: Reactive oxygen species (ROS) generation 32

Figure 3.1: Particle synthesis and composition..49

Figure 3.2: Stability, optical properties and magnetic resonance contrast effect of Gd@Cdots...51

Figure 3.3: Radical production of Gd@Cdots under radiation...53

Figure 3.4: In vitro cytotoxicity of Gd@Cdots on H1299 cells 55

Figure 3.5: Gd@Cdots showed enhanced cytotoxicity under X-ray radiation.................57

Figure 3.6: In vivo studies of Gd@Cdots 59

Figure 4.1: Optical properties and magnetic resonance contrast effect of Gd@Cdots......70

Figure 4.2: In vivo imaging studies 72

Figure 4.3: *In vivo* particle clearance study 74

Figure S1: Gd@Cdots dispersed in water 106

Figure S2: STEM image of Gd@Cdots 107

Figure S3: Statics on size distribution of Gd@Cdots, based on the TEM results 107

Figure S4: Gd release study 108

Figure S5: Gd@Cdots accumulation in mitochondria 108

Figure S6: Statistics for cell γH2AX loci numbers 109

Figure S7: Clonogenic assay with Au nanoparticles 110

CHAPTER 1

LITERATURE REVIEW: RADIATION THERAPY AND HIGH-Z NANOPARTICLES

1.1 Introduction to radiation therapy

Cancer is a major health problem worldwide and it is the second leading cause of death in the united states. About 20 % of people develop cancer, and almost 10% people die from the disease.[1] Differ to other diseases, cancer is not limited to specific organ. Instead, it can occur from all organs and cells with various reasons.[2-4] In the past decades, many research have focused on finding treatment modalities to defeat cancers, and the 5-year survival rate has been improved in many cancer types.[5-7]

One of the most common cancer treatment modalities is radiation therapy (RT). The history of RT was started from the discovery of X-ray in 1895, by a German physicist Wilhelm Conrad Roentgen.[8] After one year, Emil Herman Grubbe used X-rays to treat breast cancer which showed a promising result.[9] In 1898, Marie and Pierre Curie discovered radium as a source of radiation followed by characterizing physiologic effects of radium rays and isolating radioactive radium salts from the mineral pitchblende in 1902.[10, 11] The discovery of radium and its characteristics triggered investigations of radioactivity in cancer treatment application.[12] In early period of time, the most frequently treated cancer using X-ray and radium was skin cancer because of low tissue penetration.[8] Over the time, new devices which can emit higher energy X-ray were developed, and cancer in deeper tissue can be treated. [13, 14]

Currently, RT is an important component of cancer treatment with about 50% of the patients with cancer either as a neoadjuvant or adjuvant treatment.[15, 16] In this chapter, I would like to overview on the principle of conventional radiation therapy. Then, the mechanisms of high-Z nanoparticles in radiation therapy is introduced followed by summary of recent researches on different high-Z nanoparticles. Finally, this chapter concludes with current challenges of high-Z nanoparticles in radiation therapy and introduction of following chapters.

1.2 Principal of radiation therapy

Radiation therapy kills cancer cells in targeted area using biological effects of ionizing radiation which has enough energy to remove electrons from an atom resulting the atom in charged or ionized during the interaction.[17] Ionizing radiation includes high-energy photon radiation such as X-ray and gamma ray, and particle radiation such as alpha and beta particles, proton, and neutron beams.[18]

There are two ways to deliver radiation to tumor. Internal beam radiation therapy or brachytherapy deliver radioactive sources inside the body close to the tumor site or into the tumor in the form of wires, seeds, or rods.[19] The radioactive sources such as iodine-129, cesium-131, and iridium-192 emit radiation in form of alpha, beta, and gamma rays with a limited distance of penetration as they decay.[20-23] The brachytherapy brings benefit of delivering high dose of radiation to the local tumor tissue with minimum dose exposure to the surrounding normal tissues.[24] However, the use of high energy radioactive sources that pose a radiation safety hazard to patients or people who work with is concerned about. On the other hand, external beam radiation therapy (EBRT) directs radiation beams to the targeted tumor from outside the body using a linear accelerator, and the radiation intensity can be tuned depending on the depth of the target location.[25, 26]

When the radiation reach to cancer cells, they damage the cancer cells either by direct or indirect action.[27, 28] In the case of direct action, ionizing radiation directly interact with biomolecules such as DNA, resulting in termination of cell division and proliferation. In contrast, indirect damage is induced by secondary species such as secondary electrons or reactive oxygen species which are mainly derived as a radiolysis product of water.[29-31] Briefly, when the X-ray interacts with water molecule, positive water molecule and an electron are created. The electron joins to another water molecule forming negative water molecule and hydroxyl radical. The negative water molecule becomes a hydroxyl ion and a hydrogen radical. The hydroxyl radical often combines to form hydrogen peroxide, and the hydrogen radical combines to oxygen producing hydroperoxyl radical. The previous studies have shown that 70% of DNA damage is caused by reactive oxygen species and 30% of DNA damage is due to the secondary electrons and direct fragmentation of the DNA.[32, 33]

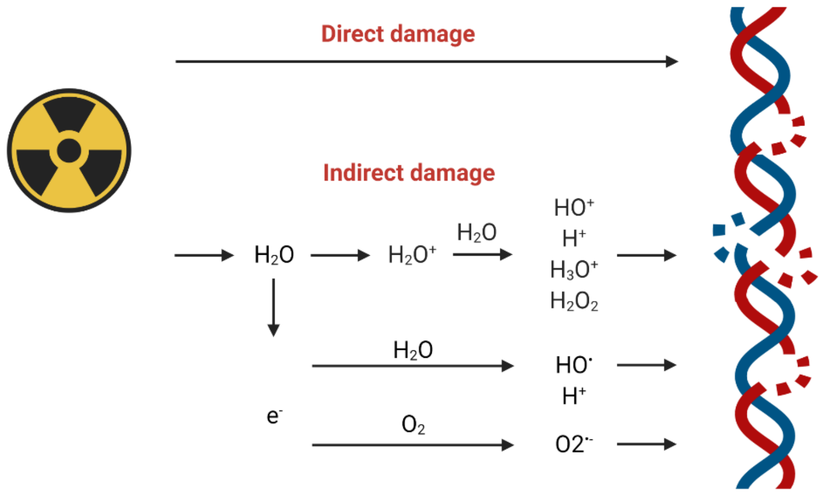

Figure 2. Principle of radiation therapy. Direct damage and indirect damage.

The DNA damage can be categorized in to three types: base damage, single strand breaks (SSBs), and double strand breaks (DSBs). [34-36] The cells may repair base damage and SSBs, and the cells continue the cell function and proliferation. In contrast, DSBs cannot be repaired, and it can cause more significant damage to the cells resulting in non-proliferation and cell death. [37] Therefore, sufficient dose of radiation is essential to damage the cancer cells. Moreover, the most solid tumors are more radio resistance, and higher dose of radiation is required to achieve the satisfied result. However, when the dose is increased, the surrounding healthy tissues are exposed to significant amount of radiation, and the increasing amount of radiation can be a double edge sword since the ionizing radiation itself is toxic. The high dose of radiation results in severe normal tissue damage which can lead life threatening. Therefore, the dose should be limited by the tolerance of normal tissues. [38, 39]

To reduce damage to the normal tissues while increasing the dose delivery to the target, multiple parameters including maximum dose tolerance of tissue, total radiation dose, fraction size, volume of exposed tissue should be considered to plan the radiation therapy. The development of imaging technique such as MRI and CT allows precise delineation of tumor shape and volume and leads to development of 3D conformal radiotherapy (3DCRT).[40, 41] 3DCRT deliver lower-energy radiation from multiple angles leading the overlap of the beams and high dose accumulation to the targeted tissue. Although this technique can reduce dose accumulation to the normal tissues, larger volume of normal tissues is exposed to the radiation.[37] To minimize dose exposure to the normal tissues, intensity modulated radiation therapy (IMRT) was introduced which uses larger number of smaller radiation beams compare to 3DCRT. By controlling the strength of the radiation beams at each location, higher radiation doses can be delivered to the tumor with less side effects allowing escalation of maximum radiation dose.[42] However, since the surrounding normal tissues on the path where the radiation penetrates, the maximum dose of radiation is still limited depending on the radiation tolerance of tissues and, sometimes, results in unsatisfactory treatment outcome.[43, 44]

To overcome the dose limitation, radiosensitizers are often used along with radiation therapy.[45] Radiosensitizers make tumor cells more sensitive to radiation, and, therefore, they can be significantly damaged with lower dose of radiation. The conventional radiosensitizers are small molecule chemotherapeutics such as gemcitabine, platinum analogs, fluoropyrimidines. They enhance the radiosensitivity of tumor cells by dysregulating cell cycle or forming interstrand DNA crosslinks which limit recovering of DNA damage caused by radiation.[46, 47] However, these small molecule radiosensitizers often cause side effects due to off targeting accumulation.[48-50] Therefore, radiosensitizers which can be delivered to target site and minimize toxicity are desired.

1.3 Principle of radiation therapy with high-Z nanoparticles

Nano-radiosensitizers or radiation dose enhancers are small synthetic particles, smaller than 100nm.[51] Compare to the conventional small molecule radiosensitizers, the Nano-radiosensitizers are easy to be manipulated in terms of size, shape, and functionalization.[51, 52] Nano-radiosensitizers can increase the dose delivered to the target tissue when they are made with elements that have large photo-absorption cross sections, or they can be used as a vesicle to carry the small molecule drugs so that the therapeutic agents are delivered to targeting area minimizing off target accumulation.

Therefore, sometimes, enhanced therapy outcome can be carried out by synergistic effect of increased radiosensitivity and enhanced energy deposition**.** [53]

High-Z nanoparticles (HZNPs) are considered as a type of Nano-radiosensitizers. The radiosensitizing effect of HZNPs was introduced when patients received treatment for mandibular and head and neck cancer with metal implants more than 30 years ago.[54-56] The radiosensitization effect by HZNPs is based on their strong capabilities for absorbing ionizing radiation leading to local dose enhancement and emitting secondary electrons which can promote reactive oxygen species generation. It is mainly by Compton scattering or photoelectric effect.[37, 57]

Compton scattering is an inelastic scattering of a photon by an electron. (Fig. 1.2a) It is caused when the incident photon interacts with outer shell electrons resulting in changing direction of incident photon and transferring the energy to the electrons.[58, 59] The probability of Compton effect is inversely proportional to photon energy and proportional to the number of electrons per grams of the material which means that most elements have similar probability.[58, 60, 61] Therefore, Compton effect is not influenced by atomic number although it still has a major role in radiation effect by increasing energy deposition at the local site.

Photoelectric effect, in the other hand, occur when the incident photon hits an electron on the internal orbit.[58] Once the photon energy is transferred to the electron, the electron is emitted from the orbit leaving an empty space, and the vacancy is filled by an electron from outer orbital.[58] While the electron is moving from outer to inner orbital, it release energy in forms of radiation. This secondary radiation can be absorbed by another electron on the outer shell causing another electron releasing which is called

Auger electron.[58] This Auger electron can be toxic to the cell because it has very high linear energy transfer (LET).[62] Unlike to the Compton effect, the probability of the photoelectric effects is directly proportional to the cube of atomic number (Z^3) and inversely proportional to the incident photon energy (E^3).[63, 64] Therefore, the HZNPs with higher atomic number element will produce more photoelectrons, secondary radiation, and Auger electrons resulting in stronger dose enhancement and focal ionization effect to the targeting sites.[63, 64]

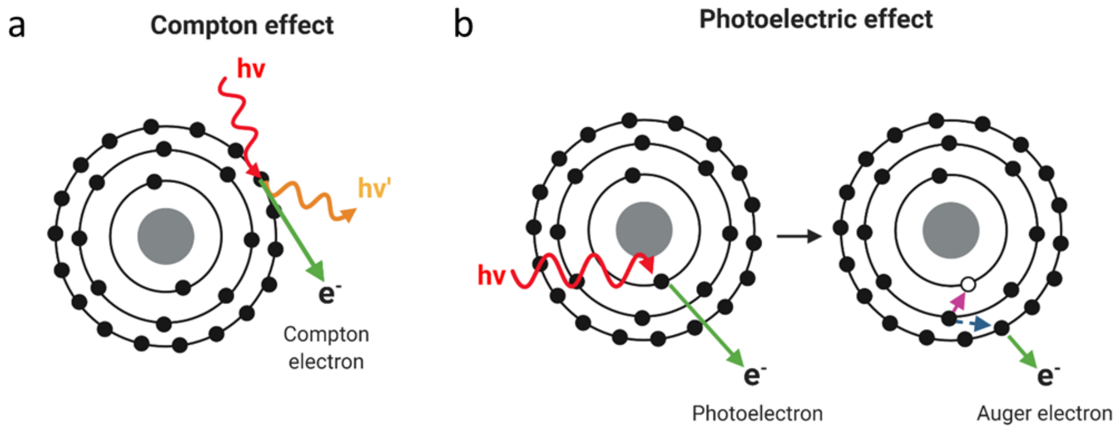

Figure 3. mechemism of does accumulation enhancement and secondary electron production by high-Z nanoparticles.

1.4 Chemical and biological effect of High-Z nanoparticles in radiation therapy

As we saw on the previous section, when the incident radiation hit HZNPs, a large number of secondary electrons are produced. These secondary electrons can either damage DNA through a dissociative electron attachment, or they can interact with water molecule to increase the reactive oxygen species production (ROS) such as hydroxyl radical (OH^*), singlet oxygen ($^1O_2$), super oxide (O_2^-), and hydrogen peroxide

(H_2O_2).[65] The ROS are highly reactive, and they induce oxidative stress and DNA damage which can cause cell death. (Fig. 1.3)

DNA damage and repair

Ionizing radiation (IR) induces DNA damage either by direct or indirect interactions. Once the DNA is damaged, DNA damage response (DDR) system is activated to repair the DNA injuries.[66] However, DNA double strand break (DSB) are difficult to repair resulting in cell death. With the increased number of secondary electron and ROS, HZNPs can induce more DNA damage to the cell.

When the DNA damage is induced, phosphorylated histone γ-H2AX and DNA repair protein 53BP1 are activated to repair DSBs.[67, 68] Moreover, it has been shown that the amount of γ-H2AX foci is directly proportional to the number of DBSs.[67] Therefore, by measuring the amount of γ-H2AX and 53BP1, the DNA damage or response to radiation exposure can be evaluated. In most studies, γ-H2AX foci is revealed by immunostaining and detected through fluorescence microscopy after 0.5-1 h irradiation.[69-71] After irradiation, the γ-H2AX foci number decreases as the DNA is repaired.[72] Therefore, by monitoring the kinetic for DNA damage and repairing over the time after irradiation, more detailed information on DBSs can be obtained. The theoretical kinetic model $N(t) = A(1 - e^{-Bt})\ (Ce^{-Dt} + (1 - C)\ e^{-Et})$ is based on the foci phosphorylation and de-phosphorylation processes where A is normalization factor, B drives the dynamic of the ionizing radiation induced foci (IRIF), C is the weight of simpler damage, D is decay rate of C, E is decay rate of (1-C).[73] Overall, this formula explains number of foci at a time after radiation exposure.

Tumorigenesis

When the cells are irradiated by ionizing radiation, they slowly lose their ability to proliferate due to DNA damage. Therefore, by testing the reproductive ability of single cell after treatment, the effectiveness of treatment can be evaluated.

The gold standard to monitor radiation treatment effect *in vitro* is clonogenic assay which was developed by Puck and Markus in 1956.[74] The clonogenic assay can evaluate and compare the reproductive viability and colony forming ability between control and different cytotoxic agents including chemotherapeutics, radiosensitizers, or nanoparticles under different radiation doses.[75] The data is presented in the survival curves plotted with the survival fraction (SF), the number of colonies formed at dose (D) divide by that of dose 0, against the radiation dose (D).[76] This experimental data is again fitted into a linear quadratic (LQ) model, $SF = e^{(-\alpha D - \beta D^2)}$, where SF is survival fraction, α is linear parameter, β is quadratic parameters in the model, and D is the radiation dose.[76] To quantify the does enhancement effect by the HZNPs, dose modifying ratio ($DMR_{x\%}$) is often calculated by the formula, $DMR_{x\%} = \frac{D_{x\%,\ cotrol}}{D_{x\%,\ HZNPs}}$.[76] This equation explains the ratio of the dose to produce the same survival level (x%). Usually, 10% survival level is used to calculate DMR since it has smaller uncertainties compare to the higher survival level.[76, 77] In many studies, survival fraction at a dose of 2Gy is evaluated since the initial slope of the survival curve is more relevant to the clinical result and 2 Gy is typical fractional dose in radiation therapy.[76, 78, 79] Therefore, sometimes, the does enhancement factor (DEF) evaluate by the ratio of doses which lead to the same levels of cell survival as the control sample at 2Gy.

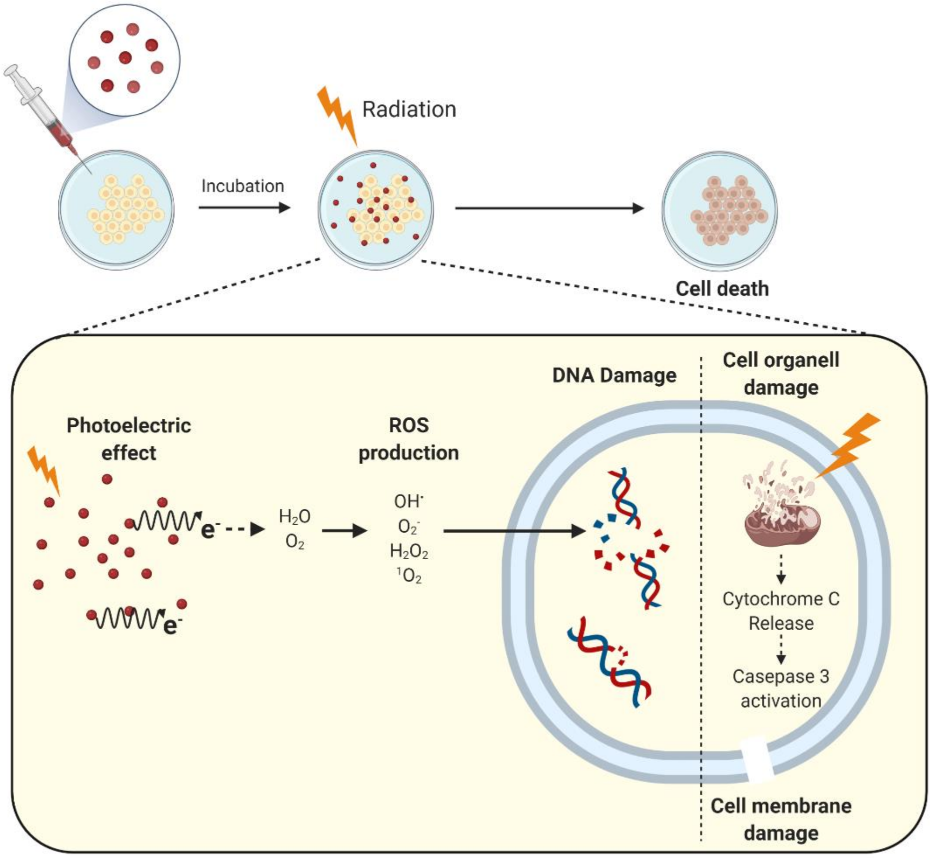

Figure 3. Scheme of impact of HZNPs to the cell. The incident radiation interacts with HZNPs and produce secondary electrons by photoelectric effect. These secondary electrons interact with water or oxygen molecules to produce ROS such as hydrogen peroxide, superoxide, singlet oxygen, and hydroxyl radicals leading DNA damage. Meanwhile, the oxidative stress on the cells also enhanced due to enhanced dose accumulation by HZNPs. The oxidative stress leads cell membrane and mitochondrial damage resulting in cell death.

1.5 Current research on high-Z nanoparticles

Until now, many studies have reported radiosensitizing effect with HZNPs using different high-Z elements including, Silver (Z=47), Gadolinium (Z=64), hafnium (Z=72), gold (Z=79), bismuth (Z=83).[53, 80-84]

Gold nanoparticles (AuNPs) have been studied for radiation therapy because gold has strong photoelectric absorption coefficient with the atomic number of 79 and good biocompatibility which can minimize toxicity.[85] In the previous studies, the size, morphology, and surface functional group affect to the radiation therapy effect.[86, 87] Liang et al. explored how the size of AuNPs affect to radiation therapy outcome. On this study, PEG coated AuNPs, range of size 4.8 nm – 46.6 nm, was tested in vitro and in vivo, and 12.1 and 27.3 nm AuNPs showed outstanding therapeutic effects compare to other size of particles. [87] Although the AuNPs showed promising result and good biocompatibility, changing properties of AuNPs by size could be a drawback in radiation therapy application. In the radiation therapy, the nanoparticle size smaller than 6 nm is ideal because of fast renal clearance, good tumor accumulation, and favorable interaction with radiation.[88, 89] However, it was shown that the AuNPs become chemically active when the size is smaller causing toxicity. Tsoli et al. found that IC_{50} of 1.4 nm AuNPs is 0.24 μM which is 180 times lower than the IC_{50} of cisplatin.[90]

Silver (Z=47) is another good candidate for HZNPs. In many studies, AgNPs showed promising result as a radiosensitizers and dose enhancer in radiation therapy.[91, 92] Zhao et al. functionalized AgNPs with PEG and an aptamer As1411 targeting glioma cancer. They reported that the systemic delivered particles can be effectively accumulated at the tumor site, and the mean survival time of C6 glioma bearing mice can be significantly increased in combination with irradiation.[92] Moreover, AgNPs have been reported for antimicrobial activity and anticancer therapeutic effect suggesting synergistic effect between chemotherapeutic effect and radiosensitizing effect. Abdellatif et al proposed that silver citrate nanoparticles (AgNPs-CIT) can inhibit TNFα expression by deactivation of the NF-κB signaling event in stimulated breast cancer cells. [93] However, compare to gold, silver has less biocompatibility, and this may cause toxicity.[94-97]

Gadolinium (Gd) has atomic number of 64, and gadolinium chelates have been used as T1 contrast agent in magnetic resonance imaging. Therefore, Gd based nanoparticles have been proposed for MRI guided radiotherapy.[98-100] Liu et al. suggested that pH-Low Insertion Peptide (pHLIP) conjugated gadolinium nanoparticles (pHLIP-GdNPs) can successfully target acidic tumor environment increasing 78-fold cellular uptake compare to GdNPs, and promotes the radiation therapeutic effect resulting in enhancement of vitro radiosensitivity by 44%.[99] Verry et al. used 3.0 ± 1 nm gadolinium based activate guided irradiation by x-ray nanoparticles (AGuIX NPs) for tumor imaging and clinical 6 MV radiotherapy in 9L-ESRF-bearing rats. The animals were treated with different concentration of NPs followed by two fractions of 10 Gy at day 10 and day 17 after tumor implantation, and the tumor volume was measured by MRI. With the study, the mean survival time was increase 134% and 84% compare to control and radiation groups respectively. [100]

Hafnium also have high atomic number, Z = 72, and hafnium oxide nanoparticles have been being tested in clinic for various cancer types including head and neck squamous cell carcinoma, Lung metastases, Liver metastases, and pancreatic cancer. [101, 102] Recently, hafnium oxide nanoparticle, NBTXR3, has been done in phase 2 and phase 3 clinical trial for soft tissue sarcoma. In this study, NBTXR3, volume equivalent to 10% of baseline tumour volume, was directly injected into the tumor and exposed to 25 fractions of 2Gy over 5 weeks. The group treated by NBTXR3 with radiation improved radiotherapy efficacy with 2-fold higher pathological complete response and 7% less adverse events compare to radiation only group. [102] Other types hafnium nanoparticles have been proposed for pre-clinical studies. [83, 84] Gong et al. functionalized Hf-nMOFs with Fe3+ to produce HfBPY-Fe to enhance radiotherapeutic effects by Fe3+-based Fenton reaction and Hf4+-induced X-ray energy conversion in tumors. [83]

Bismuth based nanoparticles (BiNPs) are suitable cancer diagnostic and X-ray radiosensitive therapeutic agents due to the high atomic number of bismuth (Bi, Z=83) and X-ray attenuation coefficient. [53, 103] Azizi et al. proposed bovine serum albumin (BSA) mediated bismuth sulfide nanoparticles functionalized with biotin and methotrexate (Bi_2S_3@BSA–Bio–MTX) to combine the chemotherapy and radiotherapy for targeting breast cancer. [53] Sometimes, the bismuth and other metals are co-doped to the particle for dual imaging as well as amplified therapeutic effect. Detappe et al. synthesized 5nm SiBiGdNPs using top-down method for dual-modality (MR and CT) contrast enhancement and radiation dose enhancement on non-small cell lung cancer model. [103] In this study, the particle was delivered by single intravenous injection (420 mg/kg), and the mice were treated with a single fraction of 10 Gy resulting in significant improvement in both tumor growth delay and survival time.

Limitation of conventional HZNPs and overview of the following chapters

As we discussed, there are many HZNPs such as gold, gadolinium, hafnium, platinum, and silver nanoparticles have been investigated in nonclinical or preclinical studies, and some HZNPs such as hafnium oxide nanoparticles and silica-based gadolinium chelated nanoparticles have recently entered clinical trials. However, there are still obstacles in HZNPs exist which limit their potential application in clinical use.

Despite of development of nanotechnology, the major issues of HZNPs is still toxicity caused by the heavy metal. Even though nanostructured formula can reduce the heavy metal toxicity, it cannot eliminate completely. For instance, Gd-chelates, which are bound to the surface of silica nanoparticles in AGuIX, may cause nephrogenic systemic fibrosis in patients with compromised renal functions and/or increased Gd deposition in the brain. 28, 29 Although the particles are made with inert materials such as gold and hafnium, they have long circulation time and takes weeks to month to be cleared out causing potential inflammation and long-term toxicity. 30, 31 Moreover, most conventional nanoparticles have size about 20-200 nm in diameter which cannot be penetrate the center of tumor, instead, they are stuck in the interstitial space causing inhomogeneous intratumoral distribution of nanoparticles. Also, these large size particles often accumulate in the liver, spleen, and capillary in normal lung tissues leading to the off-target damage and reducing therapeutic effect. 32-34

Therefore, the ideal radiosensitizers which have marginal systemic toxicity, higher enhancement, and negligible radiation dose toxicity is still desired. To overcome the limitation, we proposed a 3nm high -Z element loaded carbon dots (M@Cdots, M=high-Z element). The next three chapters discussed about the properties of M@Cdots as a potential safe radiosensitizers. On the chapter 2, synthesis methods of M@Cdots using various carbon precursors and metals are discussed followed by their physical properties including size, surface charge, stability, and *in vitro* toxicity. On chapter 3, gadolinium loaded carbon dots (Gd@Cdots) are investigated to evaluate enhanced radiation therapeutic effect. The HZNPs have unique optical properties depending on metal and carbon precursors, and they are useful to investigate *in vivo* particle distribution, clearance profile, and toxicity. (chapter 4)

CHAPTER 2

METAL LOADED CARBON NANOPARTICLE SYNTHESIS AND CHARACTERIZATION [1]

---

[1] Chaebin Lee, Jin Xie. To be submitted to ACS Nano

ABSTRACT

High-Z element nanoparticles (HZNPs) have shown the promising properties as a potential radiosensitizers. However, the conventional HZNPs have been limited in the clinical application due to slow clearance and accumulation in non-targeting tissues which can cause long term side effects. Carbon nanoparticles or carbon dots (Cdots) are 3-10 nm zero-dimensional carbon-based materials. Chemical and biological innerness of Cdots is already well known, and Cdots have been studies for biomedical applications such as diagnosis or imaging. Although many synthesis methods were explored for carbon dots, not many studies have been done on High-Z metal loaded carbon dots (M@Cdots). In this chapter, we investigated synthesis of high-Z loaded carbon dots (M@Cdots) through a hydrothermal reaction. Gadolinium or bismuth were loaded into carbon dots made with various carbon precursors including p-phenylenediamine, citric acid, and aminobenzoic acid which have different functional groups. Then, the physical properties and reactive oxygen species (ROS) production were explored and compared.

2.1 Introduction

High-Z elements can increase energy deposition of X-rays and enhance the efficacy of radiation therapy (RT). After the emergence of nanotechnology, many studies have explored High-Z element nanoparticles (HZNPs) and revealed promising properties as a potential radiosensitizers. Until now, various high-Z elements including gold, silver, bismuth, gadolinium, hafnium, and iodide were explored to synthesize HZNP radiosensitizers. However, toxicity caused by slow clearance and accumulation in non-targeting tissues is still concerned and limits in the clinical application.

Carbon nanoparticles or carbon dots (CDs) are 3-10 nm zero-dimensional carbon-based materials doped with various heteroatoms including N, S, P, and B.[1] They are built with multi-layers of graphite sheet forming a spherical shape.[2] Compare to other carbon nanomaterials such as carbon nanotubes, the surface functionalized CDs has great solubility and stability in aqueous solution.[3, 4] Moreover, many studies have been done on the biocompatibility and chemical inertness of CDs showing that CDs are not toxic, and these results attract more attention to CDs for biomedical applications.[5-8] Also, the ultrasmall size (~ 3 nm) of CDs is comparable to a small protein like insulin, and it helps CDs are protected by protein opsonization and reticuloendothelial system uptake.[9] According to the previous study, the nanoparticles smaller than 10 nm can be cleared out by renal clearance.[10, 11] Therefore, the CDs can possibly be cleared out by renal clearance within short period time minimizing long-term side effect. Furthermore, the CDs can be prepared from various inexpensive resources such as citrates and carbohydrates.[12-16]

These unique properties of CDs may bring benefits when toxic heavy metals are intercalated. Since the carbon is biologically inert, the metals are prevented from releasing even in harsh biological condition such as acidic and high ionic strength environment.[17-19] Also, since the particles are removed by renal clearance within short time, the toxicity caused by heavy metal accumulation can be prevented.[17,19] Moreover, the synergistic radio-sensitizing effect is expected by high-Z elements and carbon surface which delocalizes π electrons.[20-22] The secondary electrons, produced by photoelectric and auger effects, are trapped by carbon and transferred to oxygen molecules or surface functional groups on the CDs. This promotes production of reactive oxygen species (ROS) resulting in higher radiation therapy efficacy.

The synthesis methods for CDs are categorized into two different approaches such as top-down and bottom-up methods.[23, 24] The top-down methods start from large-sized carbon precursors such as graphite, carbon black, and graphene oxide and break them into small particles by arc discharge, laser ablation, and electrochemical oxidation methods.[25-28] However, these methods often resulted in low yield or large impurities which are difficult to remove. In contrast, bottom-up approaches synthesize the particles from molecular precursors using combustion, template, pyrolytic, chemical oxidation, microwave, and hydrothermal/solvothermal methods.[29-33] The advantage of the bottom-up approach is fabrication of surface functional groups. [23, 24, 34, 35] Depending on the carbon precursors the CDs can have different surface functional groups**.** Song et al. reported a carboxyl, carbonyl, and amine functionalized carbon dots from an aminosalicylic acid (ASA) using hydrothermal process for cell imaging and Fe3+ detection in living cells.[36]

Although many synthesis methods were explored for carbon dots, not many studies have been done on High-Z metal loaded carbon dots (M@Cdots). In 2014, Our group reported direct calcination method to synthesize gadolinium loaded carbon dots (Gd@Cdots).[17] In this study, gadolinium chelate, Gd-DTPA, was dried on a crucible followed by calcination at 300 °C for 2 h in air to prepare Gd@Cdots. Although the particle showed good r1 relaxivity and strong photoluminescence, the particle size could not be controlled leading to large particle size distribution. In next study, we proposed a template calcination method.[37] In this study, mesoporous silica nanoparticles (MSNPs) were used as template, and carbon precursor (Gd-DTPA) and gadolinium salts ($Gd(NO_3)_3*6H_2O$) was loaded to the pore by capillary effect and electro static effect. This method can control the particle size by controlling the pore size of the MSNPs. Three different particle sizes of Gd@Cdots (3, 7, and 11nm) were successfully prepared. However, this method includes multiple steps and strong acid or base to remove the silica frame. Moreover, the yield is low resulting in 10 mg from each batch. Therefore, a new synthesis method which is simple, safe, and efficient with narrow size distribution is still desired.

In this chapter, we investigated synthesis of high-Z loaded carbon dots (M@Cdots) through a hydrothermal reaction. The gadolinium or bismuth loaded carbon dots were synthesized with various carbon precursors including p-phenylenediamine, citric acid, and aminobenzoic acid which have different functional groups. The physical properties and reactive oxygen species (ROS) production was explored and compared.

2.2 Material and method

Material

p-Phenylenediamine (pPD, Sigma Aldrich, Cat# 78429), Citric acid (CA, Sigma Aldrich, Cat# 251275), Amino benzoic acid (ABA, MP Biomedical, Cat# 102569), Gadolinium nitrate hexahydrate (Gd(NO3)3•6H2O, Sigma Aldrich, Cat# 211591), Bismuth nitrate pentahydrate (Bi(NP3)3 5H2O, Sigma Aldrich, Cat# 254150), Nitric acid (JT Baker, Cat# 9601-34), Ethanol (KOPTEC, Cat# 19J14D), Dialysis membrane (Spectrum, [MWCO]=100-500), Milli-Q H2O, 3-(4,5-Dimethylthiazolyl-2)-2,5-diphenyltetrazolium bromide (MTT) (Sigma Aldrich, Cat# M2128).

Cell Culture

H1299, Human non-small lung cancer cell, was cultured following to the protocol provided by ATCC. A complete growth medium was prepared by adding 50 mL fetal bovine serum (FBS; Atlanta Biologicals, Cat#S11150) and 5 mL penicillin (Corning Cat# 30-002-CI) to 450 mL of RPMI 1640 medium (Corning, Cat# 10-104-CV). The cells were sub-cultured in every three days and stored in a Thermo Scientific Heracell 150i incubator at 37 °C. A day before the experiment, the cells were washed with PBS and collected by trypsinization (37 °C, 2 min) followed by neutralization with cell culture medium and centrifugation (1200 rpm, 5 min). The supernatant was removed, and cells were dispersed in new cell culture medium. Then, the cell density was counted using a hemocytometer (Hausser Scientific, Cat# 3200) to seed desired number of cells on the plate.

M@Cdots Synthesis (M= Gd or Bi)

Gd@Cdots

Gd@Cdots were synthesized by a hydrothermal. 1.33 mmol of $Gd(NO_3)_36H_2O$ and 1.48 mmol of carbon precursor (pPD, CA, or ABA) was dissolved in 60 mL of either ethanol or Milli-Q H_2O, and the solution was transferred to a poly(tetrafluoroethylene)-lined autoclave. After heating to 180 ^oC in the oven for 12 h, the reaction was cooled down to room temperature naturally. The raw products were centrifugated followed by purification using dialysis membrane (MWCO 500) to remove carbon biproducts and free gadolinium ions ($Gd3^+$).

Bi@Cdots

Bi@Cdots were synthesized by a hydrothermal. 1.33 mmol of $Bi(NO_3)_3$ $5H_2O$ was dissolved in 4mL 5% nitric acid. 1.48 mmol of carbon precursor (pPD, CA, or ABA) was prepared in 56 mL of Milli-Q H_2O. Two solutions are transferred to a poly(tetrafluoroethylene)-lined autoclave, and the reaction was heated up to 180 ^oC for 12h. After the reaction was cooled down to room temperature, the aggregates were removed by centrifugation, and bi-carbon products and free bismuth ions (Bi^{3+}) were removed by dialysis (MWCO 500).

Physicochemical Characterization of M@Cdots.

Transmission electron microscopy (TEM) was carried out on a FEI TECNAI 20 transmission electron microscope at 200 kV for Gd@Cdots. FEI TECNAI F30 transmission electron microscope (TEM) 300 kV was used to take both TEM and Scanning transmission electron microscopy (STEM) images for Bi@Cdots. The zeta potential and size distribution measurements were carried out on a Malvern Zetasizer Nano ZS system. Energy-dispersive X-ray spectroscopy (EDS) and element mapping were performed on a FEI Inspect F FEG-SEM equipped with EDZX EDS system to confirm Gd contents in the Cdots. Inductively coupled plasma mass spectrometry (ICP-MS) was used to analyze the Gd concentration in the sample for further study.

Optical Properties of M@Cdots

Absorption and emission spectrum

Gd@Cdots and Bi@Cdots were dispersed in Milli-Q H_2O and transferred to 96 wall plates. The absorbance was scanned between 300 - 800 nm using a BioTek Synergy MX multi-mode microplate reader. The fluorescence spectra were obtained on a microplate reader (Synergy Mx, BioTeK) with different excitations.

Physical Stability of M@Cdots (M = Gd^{3+} and Bi^{3+})

Both Gd@Cdots and Bi@Cdots were incubated in PBS at pH 7.2 to test metal release profile. The samples were kept in an incubating shaker at 37 °C. At each time point (0, 1, 2, 6, 12, and 24 h), the samples were collected and centrifugated using a micro filter unit (MWCO: 3k; Amicon® Cat# UFC800308). The solution penetrated through the membrane was analyzed using ICP-MS to evaluate free metal ions.

In vitro toxicity

The cell viability was studied with H1299 cells using the standard MTT assays. The H1299 cells were seeded on 96-well plates (8000 cells per well) 24 h prior to the experiments. M@Cdots with different concentrations (0-100 µg/mL) were added to the medium and incubated with the cells for 24 h. The MTT assay was then performed.

Reactive oxygen production

Comparison between different carbon sources

Singlet oxygen ($^1O_2$) and hydroxyl radical (·OH) were tested to compare reactive oxygen species produced by different carbon sources using Singlet Oxygen Sensor Green (SOSG, Invitrogen™, Cat# S36002) and Terephthalic Acid (TA, Sigma Aldrich, Cat# 185362), respectably. Briefly, 381.6 µM of Gd@Cdots, 2 µM of SOSG, and 16 mM of TA solution were prepared in Tris buffer. Then, 100 µL of Gd@Cdots solution and 100 µL of sensor solution (SOSG or TA) were added to black 96-well-plate (Corning Costar, Cat# 3614). The fluorescence was measured before and after irradiation with 5 Gy using 50 kV X-ray generator. The fluorescence was compared to evaluate singlet oxygen and hydroxyl radical production.

Comparison between different metals

The overall reactive oxygen species produced by Gd@Cdots and Bi@Cdots were evaluated using methylene blue. Briefly, Gd@Cdots or Bi@Cdots (381.6 µM, based on metal content, same below) and 60 µg/mL of methylene blue were prepared in Tris Buffer (pH.=7.4). 100 µL of Gd@Cdots solution and 100 µL of methylene blue solution were added to a clear 96-well-plate (Corning Costar, Cat#3599) making the final metal concentration at 190.8 µM. The absorbance of the samples were measured before and after irradiation with different dose of radiation using Synergy Mx, BioTeK. The difference was used to evaluate overall reactive oxygen species generation.

2.3 Result and discussion

Particle synthesis and composition using different metal and carbon precursors

Gd@Cdots

First, Gd@Cdots were synthesized through hydrothermal reaction. (Fig.2.1.a) Briefly, carbon precoursors (pPD, CA, or ABA) and Gd $(NO_3)_3$ were dissolved in EtOH (for pPD) or milli-Q H_2O (for CA or ABA), and the solution was transferred into a poly(tetrafluoroethylene)-lined stainless-steel autoclave. The reaction took place at 180 °C for 12 h. After reaction, we collected the nanoparticles and subjected them to dialysis against to water to remove unreacted precursors and surface-bound metals.

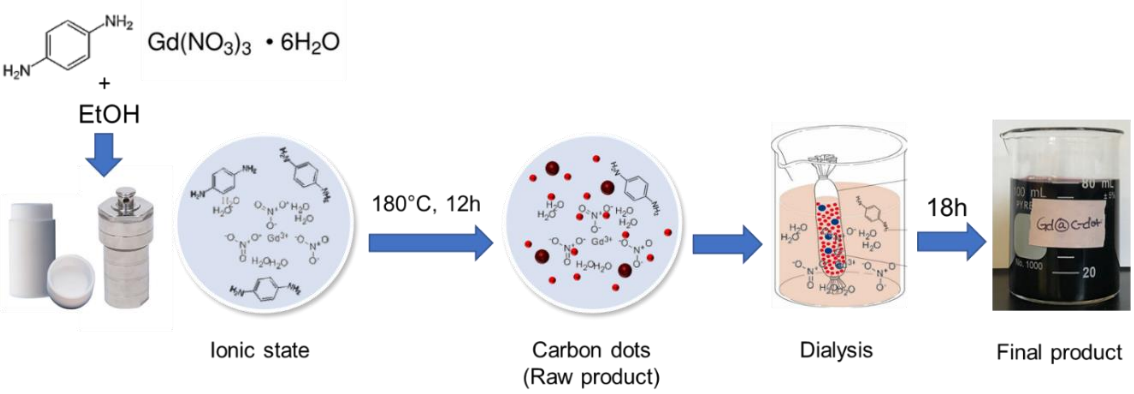

Figure 2.1 Scheme of hydrothermal reaction for M@Cdots synthesis. (M = Gd) The carbon precursors and metal salts are dissolved in 60 mL solvent. The reactor is heated up to 180 ^{0}C for 12h followed by 18 h dialysis. The final product is lyophilized and stored in -80 ^{0}C for long term storage.

The final products resulted in red, brown, and orange depending on the carbon precursors, pPD, CA, and ABA respectively. (Fig. 2.2 a) The size distribution was observed under transmission electron microscopy (TEM, Fig. 2.2 b-d). All particles synthesized with different carbon precursors resulted in spherical shape with narrow size distribution between 2-3 nm. Zeta potential analysis result showed that the functional groups on the carbon precursors can influence on the surface charge of the particles. For example, the particle synthesized with amine riche carbon precursor (pPD) have strong positive surface charge (42.3 mV) while the particle synthesized with carbon source containing carboxylic group or both amine and carboxylic groups resulted in lower surface charges, -3.78 mV, and +3.87 mV respectively. (Fig 2.2 e-g) This Then, to confirm weather the Gd was loaded to the Cdots, energy dispersive spectroscopy (EDS) was utilized. The Gd to C molar ratio was 0.101 (pPD), 0.088 (CA), and 1:0.067 (ABA) showing high Gd contents in nanoparticles. (Fig 2.2 h) The optical properties such as absorbance and fluorescence were also influenced by the carbon precursors. The Gd@Cdots made with pPD, which has amine groups, showed multiple absorbance peaks at 457 nm, 520 nm, and 570 nm, but emission peaks from those excitation wavelengths were similar (622 nm, 632 nm, and 633 nm). (Fig 2.2 i and l) When particles were synthesized with carboxylic group containing carbon precursor, CA, only one absorbance peak presented at 347 nm and emission at 449 nm. (Fig 2.2 j and m) When there are both amine group and carboxylic groups were on the carbon source (ABA), the particles showed multiple absorbance peaks at 450 nm, 475 nm, and 536 nm. (Fig 2.2 k) Interestingly, with those excitation wavelength, the different emission peaks were observed at 551 nm, 600 nm, 610 nm. (Fig 2.2 n)

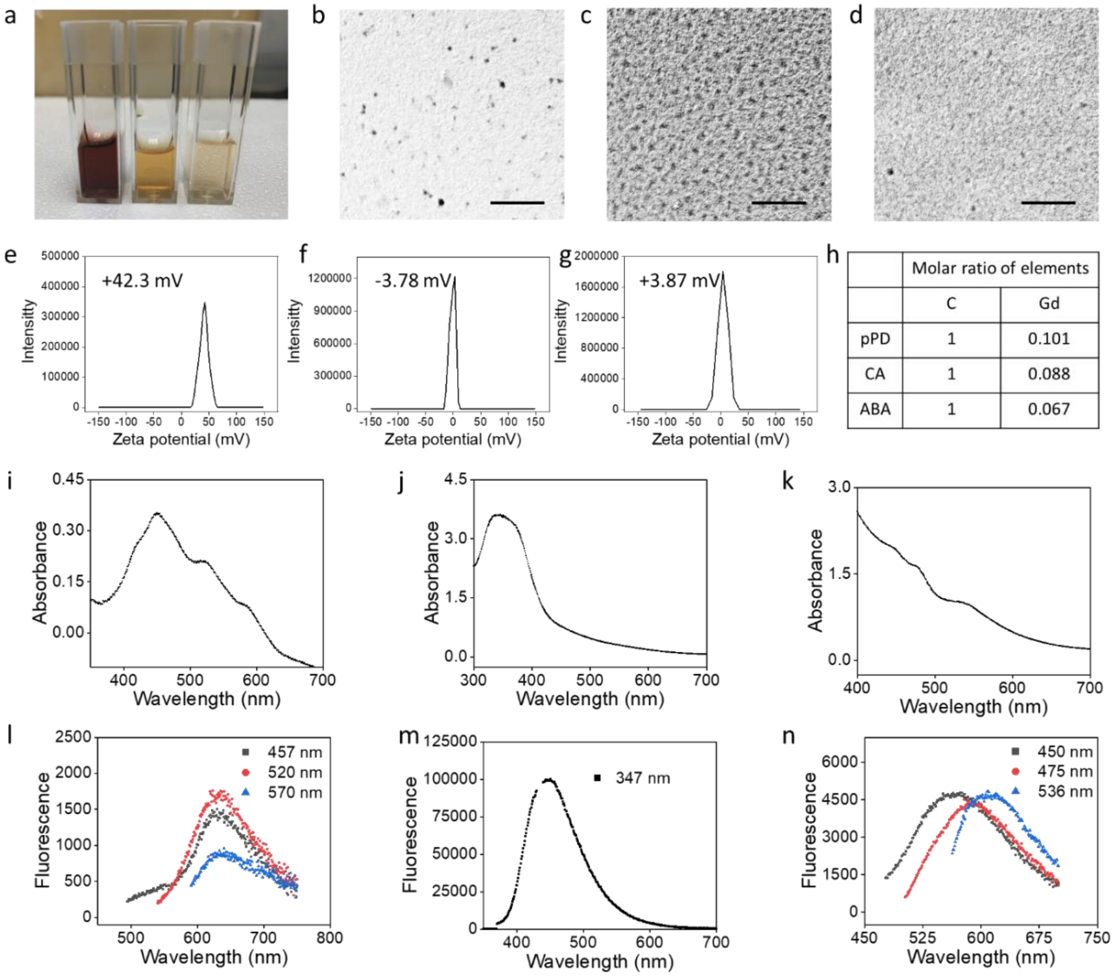

	Molar ratio of elements	
	C	Gd
pPD	1	0.101
CA	1	0.088
ABA	1	0.067

Figure 2.2 Physiochemical characteristics of Gd@Cdots. a. Final product of Gd@Cdot synthesized with different carbon precursors (left: pPD, center: CA, right: ABA). b-d. TEM images of Gd@Cdots with pPD (b), CA (c), ABA (d). h. Carbon to gadolinium molar ratio for different Gd@Cdots. e-g. Surface charge of Gd@Cdots with pPD (e), CA (f), ABA (g). i-n. absorbance and fluorescence of Gd@Cdots made with pPD (i and l), CA (j and m), ABA (k and n).

Synthesis of Bi@Cdots

After we confirmed the hydrothermal method can successfully loads metals into the carbon nanoparticles, we tried to load another metal, bismuth (Bi), into the particles. The synthesis procedure was same to that of Gd@Cdots except presence of HNO_3 to dissolve bismuth salt ($Bi(NO_3)_3$•$5H_2O$). Compare to Bi@Cdots made with pPD and ABA, the particles made with CA resulted in very low yield suggesting CA may not be able to form Cdots under acidic condition. Therefore, Bi@Cdots made with pPD and ABA were analyzed for further studies. Under TEM, both Bi@Cdots made with pPD and ABA showed 2 – 3 nm of spherical particles with narrow size distribution. (2.3 b and c) Like Gd@Cdots, the Zeta potentials on Bi@Cdot were strongly influenced by the functional groups on the carbon precursors resulting in +33.2 mV (pPD) and -1.21 mV (ABA). (Fig. 2.3 d and e) The bismuth loading efficiency was evaluated using EDS. The Bi : C molar ratio was 1: 0.239 (pPD) and 1 : 0.153 (ABA). (Fig. 2.3 f) From this result, we may confirm that the hydrothermal method can successfully load different metals to the CDs. The absorbance and fluorescence were also measured. The Bi@Cdots synthesized with pPD showed multiple absorbance peaks at 453 nm and 525 nm resulting in emission peaks at 645 nm, respectively. (Fig 2.3 g and h) The particle prepared with ABA showed single absorbance and emission peak at 535 nm and 595 nm respectively. (Fig. 2.3 i and j)

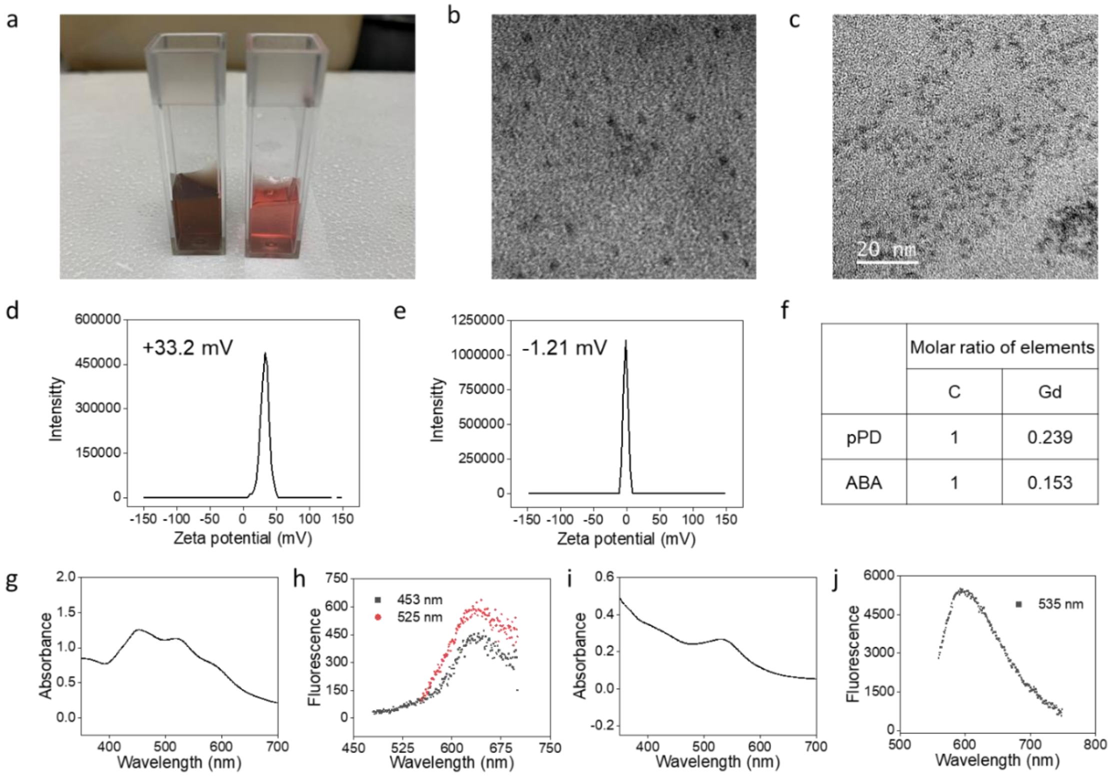

Figure 2.3 Physiochemical characteristics of Bi@Cdots. a. Final product of Bi@Cdot synthesized with different carbon precursors (left: pPD and right: ABA). b and c. TEM images of Gd@Cdots with pPD (b) and ABA (c). d and e. Surface charge of Gd@Cdots with pPD (d) and ABA (e). f. Carbon to bismuth molar ratio for different Bi@Cdots. g - j. absorbance and fluorescence of Bi@Cdots prepared with pPD (g and h) and ABA (i and j).

Stability of M@Cdots and *in vitro* toxicity

The stability of Gd@Cdots and Bi@Cdots were tested by analyzing Gd^{3+} and Bi^{3+} released from the nanoparticles. In both neutral and acidic solutions (pH = 7.2 and 5.4, respectively), less than 1% Gd and Bi were released over 24 h incubation. (Fig. 2.4 a and b) With the negligible amount of metal release confirms that the metals and carbon can bind strong enough. Then, we tested in vitro toxicity to confirm if the minimal metals leakage can prevent cells from metal toxicity. With 24 h MTT study with H1299 cell line, there were no toxicity showed up to 100 μg/mL of Gd@Cdots and Bi@Cdots based on metal concentration. (Fig. 2.4 b and c)

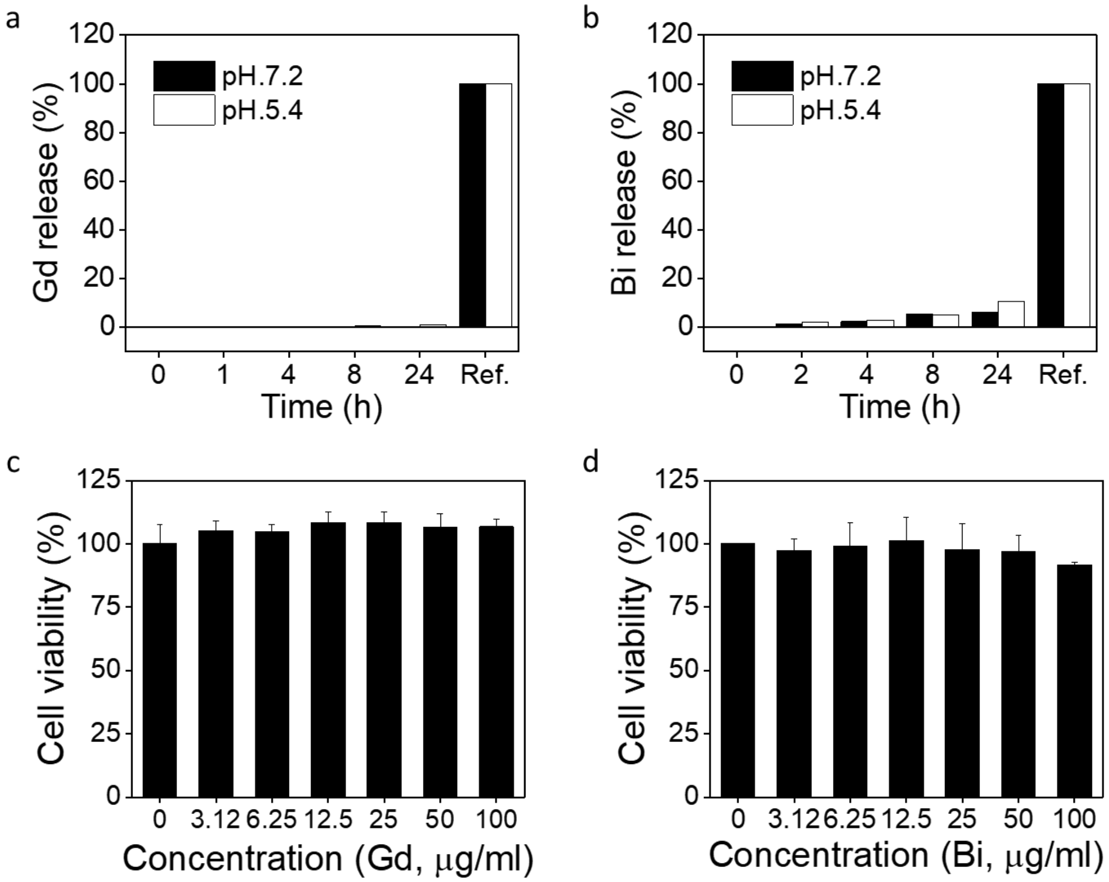

Figure 2.4 a and b. Gd^{3+} and Bi^{3+} released from Gd@Cdots and Bi@Cdots in neutral and acidic solution (pH 7.2 and 5.4) at 37 ºC for 24 h. The released Gd^{3+} and Bi^{3+} were analyzed using ICP-MS. c and d *in vitro* toxicity study with Gd@Cdots(c) and Bi@Cdots (d).

Reactive oxygen species generation

The reactive oxygen species produced by each particle was evaluated and compared. First, to compare between different carbon precursors, we tested hydroxyl radical and singlet oxygen generation under presence of 5Gy.(Fig 2.5 a and b) The result showed the Gd@Cdots synthesized with pPD produced the least hydroxyl radical and singlet oxygen, and the particle synthesized with ABA produced the largest amount of reactive oxygen species. This result suggests that more negatively charges nanoparticle may produce larger amount of ROS. Next, ROS produced between Gd@Cdots and Bi@Cdots were compared using methylene blue assay which can evaluate overall ROS production. (Fig 2.5 c and d) Both Gd@Cdots and Bi@Cdots were prepared in methylene blue solution making the final metal concentration at 190.8 µM. After irradiated the samples with different X-ray doses (0-8 Gy) using both 50 kV and 6 MV accelerator, the ROS difference of absorbance was plotted against to the dose to compare the ROS production by each sample. The result showed that under 6 Gy with 50 kV, the ROS production was increased by 121.1 % and 242.9 % with both Gd@Cdots and Bi@Cdots respectively. Since the atomic number of Bi (Z = 83) is higher than the atomic number of Gd (Z = 64), it has stronger photoelectric effect generating more photoelectric and auger electrons. Therefore, Bi@Cdots can enhance the radiation effect more than Gd@Cdots producing larger amount ROS.

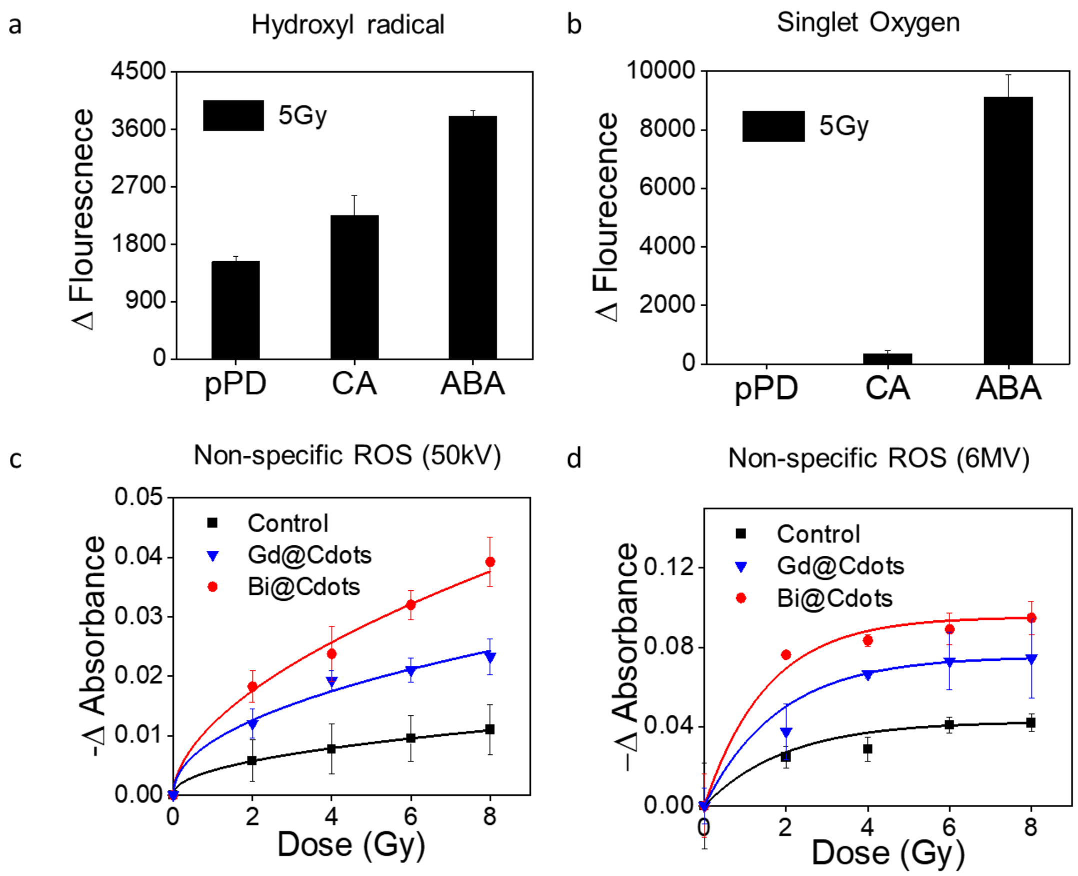

Figure 2.5 Reactive oxygen species (ROS) generation a. Hydroxyl radical generation by three types of Gd@Cdots under 5 Gy X-ray. b. Singlet oxygen generation by three types of Gd@Cdots under 5 Gy X-ray. c,d. Overall ROS generation by contol, Gd@Cdots, and Bi@Cdots made with pPD under presence of X-ray (0 – 8 Gy).

2.4 Conclusion

Until now, many methods for carbon dot synthesis have been explored. However, not many studies were done on the metal loaded carbon nanoparticles. Here, we loaded Gd and Bi to carbon dots with different carbon sources (pPD, CA, and ABA). The results showed the metal loading does not significantly affect to the carbon properties such as size, surface charge, absorbance, and fluorescence. Instead, depending on which carbon precursors are used, the physical characteristics can be tuned. Moreover, the M@Cdots showed less than 1% Gd release and 8% Bi release suggesting the metal and carbon are strongly bound. With this high stability, the in vitro toxicity was negligible up to 100 μg/mL for both Gd@Cdots and Bi@Cdots.

CHAPTER 3

ULTRASMALL Gd@Cdots AS A RADIOSENSITIZING AGENT FOR NON-SMALL CELL LUNG CANCER [2]

---

[2] Chaebin Lee, Xiangji Liu, Weizhong Zhang, Michael A. Duncan, Christine Kim, Xuefeng Yan, Yong Teng, Hui Wang, Wen Jiang, Zibo Li, Jin Xie. To be submitted to Nanoscale

ABSTRACT

High-Z nanoparticles (HZNPs) are an emerging type of radiosensitizing agent. Conventional metal or metal oxide HZNPs can increase energy deposition in tumors, leading to enhanced cancer cell death during radiotherapy (RT). However, these nanoparticles are often associated with issues such as suboptimal pharmacokinetics, low cellular accumulation, and heavy metal toxicity. Herein, we investigate ultrasmall gadolinium encapsulated carbon dots (Gd@Cdots) as a novel type of radiosensitizer. Possessing high-Z dopants and an electronically active carbon shell, Gd@Cdots can efficiently enhance radical production under irradiation. Meanwhile, carbon is biologically inert and can efficiently prevent metal leakage. This, in conjugation with renal clearance of ultrasmall nanoparticles, reduces the risks of systemic toxicity. Gd@Cdots were tested *in vitro* and then *in vivo* with non-small cell lung carcinoma (NSCLC) xenograft models. Our data suggest that intraveneously injected Gd@Cdots can accumulate in tumors and significantly sensitize cancer cells to RT, without causing normal tissue or hematologic toxicities.

3.1 Introduction

High-Z nanoparticles (HZNPs) as a novel type of radiosensitizers have attracted wide attention [1-3]. Affording high photoelectric effects, HZNPs can increase the production of photo- and Auger-electrons, and enhance the efficacy of radiotherapy (RT) [4-9]. For instance, a number of groups have reported that gold nanoparticles can boost cellular damage under kV and clinical MV beams [7, 10-11]. Hafnium oxide nanoparticles (NBTXR3) and Gd-chelate-bound silica nanoparticles (AGuIX) are being tested in the clinic, and the initial results are encouraging [4, 12]. Bi-, Pt-, and W-containing HZNPs have also been synthesized and investigated [5, 8-9, 13-16]. Despite the promise, toxicity remains a major concern for HZNPs. Many HZNPs are stable in the short-term but degrade inside cells, releasing toxic heavy metals. Meanwhile, HZNPs made from inert metals or metal oxides may stay for months or even years in the host [17], and their long-term impacts remain to be fully investigated. Moreover, many conventional HZNPs have relatively bulky sizes (e.g. 20-200 nm in diameter), limiting their accumulation and migration in tumors as well as uptake by cancer cells. It is commonplace to inject HZNPs in an intratumoral rather than systemic manner. This, however, would prevent HZNPs' use in patients in advanced stage.

Herein we explored ultrasmall Gd-intercalated carbon dots, or Gd@Cdots, as a novel type of radiosensitizer. Our groups and others have synthesized Gd@Cdots and investigated them as a magnetic resonance imaging (MRI) contrast agent [18-21]. To our knowledge, few efforts have been made on exploiting Gd@Cdots in RT. We postulate that Gd@Cdots afford strong radiosensitizing effects, which come from not only the photoelectric effects of the high-Z payloads (Gd), but also an electronically active carbon shell that facilitates water radiolysis. We expect that under beam radiation, Gd@Cdots can improve the production of reactive oxygen species (ROS), boosting RT-induced cellular damage. Meanwhile, we anticipate minimal side effects from Gd@Cdots. This is because the carbon shell, while being electronically active, is biologically inert [22] and can prevent Gd from leaking to the surroundings. Due to ultrasmall sizes, Gd@Cdots are efficiently excreted through renal clearance [19], which also helps minimize nanoparticle toxicities.

We tested these hypotheses first *in vitro* and then *in vivo* in mice bearing non–small cell lung cancer (NSCLC) tumors. We postulated that intravenously (i.v.) injected Gd@Cdots can efficiently accumulate in tumors through the enhanced permeability and retention (EPR) effect; with external beam radiation, these nanoparticles would boost cellular damage to cancer cells, leading to enhanced RT efficacy. NSCLC is diagnosed in more than 187,000 persons each year in the US and is a leading cause of cancer-related mortality [23]. RT is the standard care for the majority of NSCLC patients with locally advanced (T3-4) or local regional disease (N2-N3), which accounts for ~50% of newly diagnosed NSCLC cases. Despite technological advances, the rates of local failure in stage III NSCLC have remained high (30-40%) [24]. Increasing radiation doses does not improve survival and may be harmful (RTOG0617) [25]. Therefore, there is an urgent need for radiosensitizers that can selectively enhance RT against NSCLC.

3.2 Materials and Methods

Materials

P-phenylenediamine (pPD) (Sigma Aldrich, Cat# 78429), gadolinium nitrate hexahydrate ($Gd(NO_3)_3·6H_2O$, Sigma Aldrich, Cat# 211591), ethanol (KOPTEC, Cat# 19J14D), dialysis membrane (Spectrum, MWCO=100-500), Milli-Q H_2O, 3-(4,5-dimethylthiazolyl-2)-2,5-diphenyltetrazolium bromide (MTT) (Sigma Aldrich, Cat# M2128).

Gd@Cdots Synthesis

Gd@Cdots were synthesized by a hydrothermal method following our previous publication.[18] Briefly, 0.16 g of pPD and 0.6 g of $Gd(NO_3)_3$ were dissolved in 60 mL EtOH, and the solution was transferred into a 100 ml poly(tetrafluoroethylene)-lined stainless steel autoclave. The reaction was heated at 180 °C for 12 h and cooled down to room temperature. The resulting dark red suspension was purified using dialysis membrane (MWCO 500) against to Milli-Q water for 17 h to remove bi-carbon products and extra Gd^{3+} free ions. The final product was freeze dried for further experiment and long-term storage.

Physical characterizations

Transmission electron microscopy (TEM) was carried out on a FEI TECNAI 20 transmission electron microscope at 200 kV. The absorbance and fluorescence spectra were obtained on a BioTek Synergy MX multi-mode microplate reader. Scanning transmission electron microscopy (STEM) image was obtained using FEI G2 TECNAI F30 at 300 kV. The zeta potential and size distribution measurements were carried out on a Malvern Zetasizer Nano ZS system (Zeta potential +33.3mV, DLS 2.01nm). Energy-dispersive X-ray spectroscopy (EDS) and element mapping were performed on a FEI Inspect F FEG-

SEM equipped with EDZX EDS system to confirm Gd contents in the Cdots. Inductively coupled plasma mass spectrometry (ICP-MS) was used to analyze the Gd concentration in the sample for further study.

Mass spectrum analysis

We collected the mass spectra using both laser desorption ionization (LDI) and electrospray ionization (ESI) mass spectroscopy. ESI mass spectroscopy was performed on a Waters LCT Premier mass spectrometer. MassLynx was used as the software to collect spectra. Each ESI mass spectrum shown in this work was an average of 55 mass spectra collected in 1 minute with 0.1 second between every two one-second scans. Samples were diluted about 10 times before injection. For LDI measurements, we used the linear mode of the Comstock RTOF-210 mass spectrometer with a pulsed Nd:YAG laser at 355 nm (New Wave Research Polaris II). The laser power was less than 400 µJ/pulse. All the LDI mass spectra exhibited here were averaged from 200~500 scans. Sample solutions were applied to a solid copper tip, dried in air to form a thin film, and then inserted into the ion source.

Physical stability of Gd@Cdots

The Gd@Cdots were incubated in PBS at different pH (pH = 5.0 and 7.2) to test the stability of the particles and the release of Gd^{3+}. The samples were kept in an incubating shaker at 37 °C. At each time point (0, 0.5, 1, 2, 4, 8 and 24 h), sample solutions were collected and centrifugated on micro-filter units (MWCO: 3k; Amicon® Cat# UFC800308). Solutions passing through the membrane was analyzed by ICP-MS to evaluate free Gd^{3+}.

Optical properties of Gd@Cdots

Gd@Cdots were dispersed in Milli-Q H_2O (100 µg/mL) and transferred to a quartz cuvette. Absorbance between 200-800 nm was scanned on a Varian Cary 300 bio UV-visible spectrometer. For emission spectrum, Gd@Cdots were dispersed in Milli-Q H_2O (100 µg/mL) and placed in a black 96-well plate (Corning Costar, Cat# 3614). The fluorescence spectra were acquired on a microplate reader (Synergy Mx, BioTeK) with excitation at 457, 520, and 570 nm.

MRI phantom studies

MRI phantom samples were prepared by dispersing Gd@Cdots (0-0.1 mM) in 1% (w/w%) agarose gel. T_1 and T_2 images were acquired on a Varian Magnex 7 Tesla scanner. For T_1-weighted images, a T_1 inversion recovery fast spin echo (FSE) sequence was used using the following parameters: TR = 5000 ms, ESP = 7.69, Segment/ETL = 32/8, Effective TE = 30.75 ms, inversion times (TI) = 10.00-1500.0 ms with array size of 8, 256 × 256 matrices. For T_2-weighted images, a FSE sequence was used with following parameters: TR = 2000 ms, TE = 8.00 ms, NE = 12, 256 × 256 matrices.

Reactive oxygen species analyses

Overall ROS generation was evaluated using methylene blue assay. Briefly, a series of Gd@Cdots (20, 60, and 120 µg/mL, based on Gd content, the same below) and 60 µg/mL of methylene blue were prepared in Tris Buffer (pH = 7.4). A 100 µL solution of Gd@Cdots and a 100 µL solution of methylene blue were added to a 96-well plate (Corning Costar, Cat#3599), making the final Gd concentrations being 10, 30, and 60 µg/mL. The initial absorbance was measured on a microplate reader (Synergy Mx, BioTeK). The Gd@Cdots methylene blue solution was irradiated with 5 Gy X-ray. The absorbance after irradiation was measured and compared to the initial absorbance. The difference was computed and used to evaluate overall reactive oxygen species generation.

Singlet oxygen ($^1O_2$) and hydroxyl radical (·OH) were measured using Singlet Oxygen Sensor Green (SOSG, Invitrogen™, Cat# S36002) and Terephthalic Acid (TA, Sigma Aldrich, Cat# 185362), respectably. Briefly, a series of Gd@Cdots (20, 60 and 120 µg/mL), 2 µM of SOSG, and 16 mM of TA solution were prepared in Tris buffer solutions. A 100 µL solution of Gd@Cdots, and a 100 µL chemical sensor solution (SOSG or TA) were mixed and added to a 96-well plate (Corning Costar, Cat# 3614); the final Gd concentrations were 10, 30 and 60 µg/mL. The initial fluorescence was measured on a microplate reader (Synergy Mx, BioTeK). The Gd@Cdots solutions received 5 Gy irradiation and the fluorescence was measured again. The variation in fluorescence intensity was computed to evaluate singlet oxygen and hydroxyl radical production. To test whether the surface chemical functional groups of Gd@Cdots facilitate radical production, nanoparticles were incubated in solutions containing 0.1% Triton X-100 before mixing with TA and receiving irradiation.

Cell uptake studies

H1299 cells, which originated from human non-small lung cancer tumors, were cultured by following a protocol provided by ATCC. Gd@Cdots co-localization in the lysosome and mitochondria were tested using LysoTracker™ Green DND-26 (ThermoFisher, Cat# L7526) and MitoTracker™ Green FM (ThermoFisher, Cat# M7514), respectably. Briefly, 1×10^6 of H1299 cells were seeded on 2-chamber glass slide (Nunc™ Lab-Tek™ II Chamber Slide™ System, ThermoFisher) and incubated with Gd@Cdots at 37 °C for 4 h. After the cells were washed with PBS for 3 times, 20 nM LysoTracker or MitoTracker was added to stain the lysosome or the mitochondria for 30 min, respectably. The cells were fixed with 4% formaldehyde, and cell nuclei were stained with DAPI. Fluorescence images were taken on a Zeiss LSM 710 Confocal Microscope with 40× magnification.

Scanning transmission electron microscopy

To study the intra-cellular distribution of the particle, cells were also imaged by scanning transmission electron microscopy (STEM, FE-SEM FEI Teneo). Briefly, H1299 cells were incubated with Gd@Cdots for 4 h. The cells were collected, fixed with glutaraldehyde, and sectioned into thin slices. Resulting samples were loaded onto a carbon grid. The distribution of Gd@Cdots was evaluated on a FE-SEM Thermo Fisher Teneo system with EDS mapping.

Cytotoxicity

Cell viability was studied with H1299 cells using standard MTT and ATP bioluminescence assays. For MTT assays, H1299 cells (8000 cells per well) were seeded onto a 96-well plates (Corning Costar, Cat#3599). When cells were attached, Gd@CDots at a final concentration of 0-207.6 µg/mL were added into the wells and incubated with cells for 24 h. A 20 µL solution of 10 mg/mL 3-(4,5-dimethylthiazolyl-2)-2,5-diphenyltetrazolium bromide was added into each well. After 4 h, the solution was aspirated, and 100 µL of DMSO was added to each well. The absorbance at 570 nm was measured on a BioTek Synergy MX multi-mode microplate reader. For ATP assays, cells were incubated with Gd@Cdots (60 µg/mL), Cdots (60 µg/mL), or PBS for 4 h, followed by 5 Gy irradiation. After 24 h incubation, the supernatant was completely removed, and 55 µL cell culture medium and 55 µL ATP kit solution were added. Solution from each well was transferred to a new, opaque 96-well plate and luminescence signal was measured on a microplate reader (Synergy Mx, BioTeK). The result was compared to a standard curve established according to the manufacture's protocol.

Mitochondrial membrane potential ($\Delta\Psi_m$)

$\Delta\Psi_m$ change was assessed by JC-1 staining (Biotium, Cat# 30001). The JC-1 working solution was prepared by adding 10 µL of the concentrated dye to 1 mL of FBS free RPMI medium. 200 µL of cell culture medium containing Gd@Cdots (30 µg/mL) or PBS was incubated with cells for 4 h. The cells were irradiated with 5 Gy and incubated for 24 h. The medium was removed and replaced with the JC-1 working solution. After 15 min incubation, the fluorescence signals of the stained cells were measured on a microplate reader (green: ex/em 510/527 nm; red: ex/em 585/590 nm), and the green-to-red fluorescence intensity ratio was computed.

Cytochrome *c* release

Cytochrome *c* release was evaluated using ApoTrack™ Cytochrome *c* Apoptosis ICC Antibody Kit (Abcam, Cat# ab110417). Briefly, 1×10^6 of H1299 cells were seeded onto 2-well chamber slide for attachment. The cells were then incubated with Gd@Cdots (30 µg/mL) or PBS for 4 h before receiving 5 Gy irradiation. After 24 h, antibody was added following the manufacture's protocol. Images were taken on a Zeiss LSM 710 Confocal Microscope and analyzed by ImageJ.

Caspase-3 activity

For caspase-3 activity measurement, H1299 cells were incubated with Gd@Cdots (30 µg/mL) or PBS for 4 h, followed by 5 Gy irradiation. After 24 h incubation, cells were stained using FAM-FLICA® Caspase-3/7 kit (Immunochemistry, Cat# 94) following the manufacturer's protocol. The caspase-3 activity was evaluated by measuring fluorescence signals (ex/em: 488/530 nm) on a microplate reader (Synergy Mx, BioTeK).

Lipid peroxidation assay

Image-iT Lipid Peroxidation Kit (Abcam, Cat# ab118970) was used to assess lipid peroxidation. Briefly, cells were pre-seeded onto a 96-well plate and incubated with Gd@Cdots (30 µg/mL), Cdots (30 µg/mL), or PBS at 37 °C for 24 h. After replenishing medium, cells received 5 Gy irradiation. After 24 h, cells were stained with Image-iT Lipid peroxidation sensor (30 µM) for 30 minutes at 37 °C, and washed with PBS for three times. The yellow and green fluorescence intensities (ex/em: 581/591 nm and 488/510 nm, respectively) were recorded on a microplate reader (Synergy Mx, BioTeK), and the ratio between them was computed.

rH2AX assay

The DNA damage was evaluated using anti-rH2AX (Alexa 647) antibody (Millipore Sigma, Cat# 07-164-AF647). Briefly, H1299 cells were pre-seeded onto a 35-mm cell culture dish and incubated with Gd@Cdots (30 µg/mL), Cdots (30 µg/mL), or PBS. After 4 hour incubation, cells received 5 Gy irradiation and continued incubation for another 1 h at 37 °C. The cells were then collected, fixed, and permeabilized, and stained with anti-rH2AX antibody according to the protocol from the manufacture. Cells with positive anti-rH2AX stain was analyzed using a Millipore Sigma ImageStream X Mark II Imaging Flow Cytometer.

Clonogenic assay

Briefly, H1299 cells were pre-seeded onto a 35-mm cell culture dish (Corning, Cat# 430165) and incubated with Gd@Cdots (10 µg/mL) or PBS for 12 h. After washing, cells were collected and seeded (100-10000 cells, depending on the radiation dose) onto a 100-mm plate (Falcon, Cat# 353003), and irradiated (0-10 Gy). After 14 days, colonies were stained with crystal violet and counted. Data were fit into the linear-quadratic model: $S(D)/S(0) = \exp(-(aD+bD^2))$, where S is cell survival fraction, D is radiation dose, and a&b are fitting coefficients.

***In vivo* radiation therapy**

In vivo therapy studies were performed on H1299 subcutaneous tumor models established on 4-week-old female nude mice purchased from Charles River. All animal experiments were performed according to a protocol approved by the Institutional Animal Care and Use Committee (IACUC) of the University of Georgia. The tumor model was developed by subcutaneous injection of 2.5×10^6 H1299 cells into the right flank of mice. When the tumor size reached 100 mm^3, the mice were randomly divided into three groups (PBS, PBS+RT, and Gd@Cdots+RT). The radiation was delivered through an X-RAD 320 system. Gd@Cdots were intravenously injected (0.1 mmol/kg, 200 µL); after 4 hours, tumors received 6 Gy radiation, with the rest of the animal body lead-shielded. The tumor size was measured every 2 days with a caliper, and the tumor volume was calculated using the equation: $\text{tumor volume} = (\text{tumor length} \times \text{tumor width}^2)/2)$. The mice were euthanized when a humane end point was reached. Tumors and major organs such as the brain, liver, heart, lung, intestine, kidney, and spleen were collected for hematoxylin and eosin (H&E) and TUNEL staining.

Complete blood counts and biochemistry analysis

In a separated experiment, three balb/c mice were intravenously injected with PBS or Gd@Cdots (0.1 mmol Gd/kg). Blood samples were collected using a cardiac puncture blood collection method. 250 µL of blood samples was subjected for complete blood counts. The remaining blood samples were used to evaluate liver and kidney function using Alanine Aminotransferase (ALT) ELISA kit (Abcam, Cat# ab105134) and Urea Nitrogen (BUN) detection kit (Arbor Assays, Cat# K024H1), respectively.

Statistical analysis

Graphpad Prism 8 software (GraphPad Software, San Diego, CA) was used for statistical analysis. For reactive oxygen species studies and all the *in vitro* studies, data were expressed as mean ± standard deviation. For *in vivo* study, each group had 5 animals (n = 5). Statistical significance was evaluated by one-way ANOVA or two-way ANOVA with multiple comparison. The statistical significance was set at $^*p < 0.05$.

3.3 Results and discussion

Particle synthesis and composition

Gd@Cdots were synthesized through hydrothermal reaction. Briefly, p-phenylenediamine (pPD) and $Gd(NO_3)_3$ were dissolved in EtOH, and the solution was transferred into a poly(tetrafluoroethylene)-lined stainless-steel autoclave. The reaction took place at 180 °C for 12 h. After reaction, we collected the nanoparticles by centrifugation and subjected them to dialysis to remove unreacted precursors and surface-bound metals. The purified products were re-suspended in water, forming as a clear, dark-red solution (Fig. S1 in the ESM).

The size and morphology of nanoparticles were analyzed by transmission electron microscopy (TEM, Fig. 3.1a) and scanning transmission electron microscopy (STEM, Fig. S2 in the ESM). The average nanoparticle size was 2.60 nm, with narrow size distribution (Fig. S3 in the ESM). Dynamic light scattering (DLS) found an average hydrodynamic size of 2.04 nm and a polydispersity index (PDI) of 0.364 (Fig. 3.1b). Zeta potential analysis showed that the nanoparticle surface was positively charged (+33.3 mV, Fig. 3.1c), which is attributed to amine groups inherited from pPD.

The composition of Gd@Cdots was investigated by energy dispersive spectroscopy (EDS, Fig. 1(d)). It was found that Gd content was high in the nanoparticles, with the Gd:C molar ratio being 1:0.09 (Fig. 3.1d). Moreover, significant N was present in the particles (N:C molar ratio is 1:0.19), which was mainly attributed to the surface amine. We further probed the nanoparticle composition by mass spectroscopy (MS) using a time-of-flight (TOF) detector. Figure 3.1e shows the mass spectra of Gd@Cdots after both laser desorption and electrospray ionizations. Oxidized Gd clusters were detected and were assigned to GdC_2^+ clusters or their water/N_2 solvated clusters (Fig. 3.1e). It is worth mentioning that fragmentation of carbon species such as fullerenes is commonly associated with successive losses of C_2 units [26-27]. It is reasoned that Gd had been tightly bound to the carbon matrix, which was fragmented during ionization to form clusters such as GdC_2.

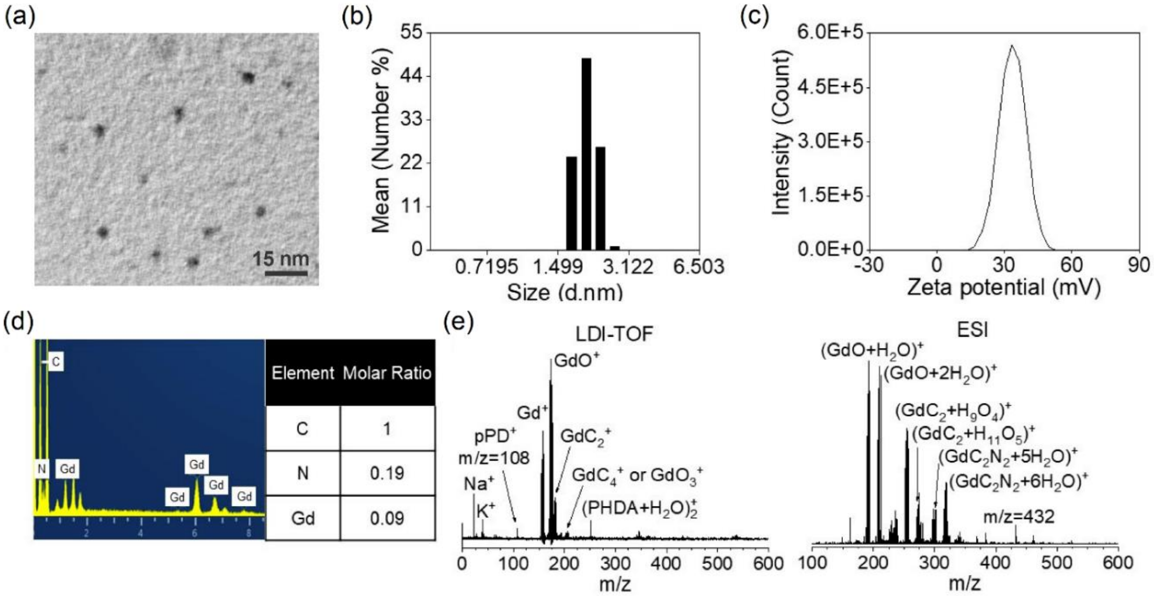

Element	Molar Ratio
C	1
N	0.19
Gd	0.09

Figure 3.1 Particle synthesis and composition (a) A representative TEM image of Gd@Cdots showing the morphology and particle size. The average particle size was 2.60 nm by measuring 100 particles on TEM image in Figure S1 in electron supplementary material. (b) Hydrodynamic size of Gd@Cdots (2.04 nm) and size distribution by Dynamic Light Scattering. (c) Zeta potential analysis of Gd@Cdots performed in Milli-Q H_2O confirmed the nanoparticle surface was positively charged (+33.3 mV). (d) Elemental composition of Gd@Cdots by EDS elemental analysis, including EDS spectrum of Gd@Cdots (left) and Element weight composition (%) (right). (e) Mass spectrum of Gd@Cdots analyzed using LDI-TOF (left) and ESI (right). The representative peaks were assigned with prospective elements.

Stability, optical properties and magnetic resonance contrast effect of Gd@Cdots

The stability of Gd@Cdots was assessed by analyzing Gd^{3+} released from the nanoparticles. In both neutral and acidic solutions (pH = 7.0 and 5.0, respectively), less than 1% Gd was released over 24 h incubation (Fig. 3.2(a)). Similarly, minimal Gd^{3+} leakage was observed in serum or 1 mM glutathione (GSH, Fig. S4 in the ESM). The high resistance was attributed to a robust carbon coating that effectively prevents Gd escape.

Gd@Cdots show strong absorbance at 457, 520, and 570 nm (Fig. 3.2(b)). This is different from Gd@Cdots or Cdots made from direct calcination, which are often amorphous and show broad absorbance across the visible spectrum window [28]. Gd@Cdots also show intense fluorescence at ~ 635 nm (Fig. 3.2(c)), which remains strong and stable in serum or GSH solutions (Fig. 2(d)). The magnetic properties of Gd@Cdots were assessed through a phantom study (where nanoparticles were dispersed in 1% agarose gel at elevated concentrations) on a 7T magnet (Fig. 3.2(e)**)**. Gd@Cdots caused concentration-dependent signal increase on T_1 images. Based on region of interest (ROI) analysis and linear regression fitting, it was determined that the r_1 relaxivity of Gd@Cdots was 19.6 $mM^{-1}s^{-1}$, and the r_2 to r_1 ratio was 2.87 (Fig. 3.2(f)). Overall, these data suggest the potential of Gd@Cdots as a dually functional imaging probe for fluorescence and MRI.

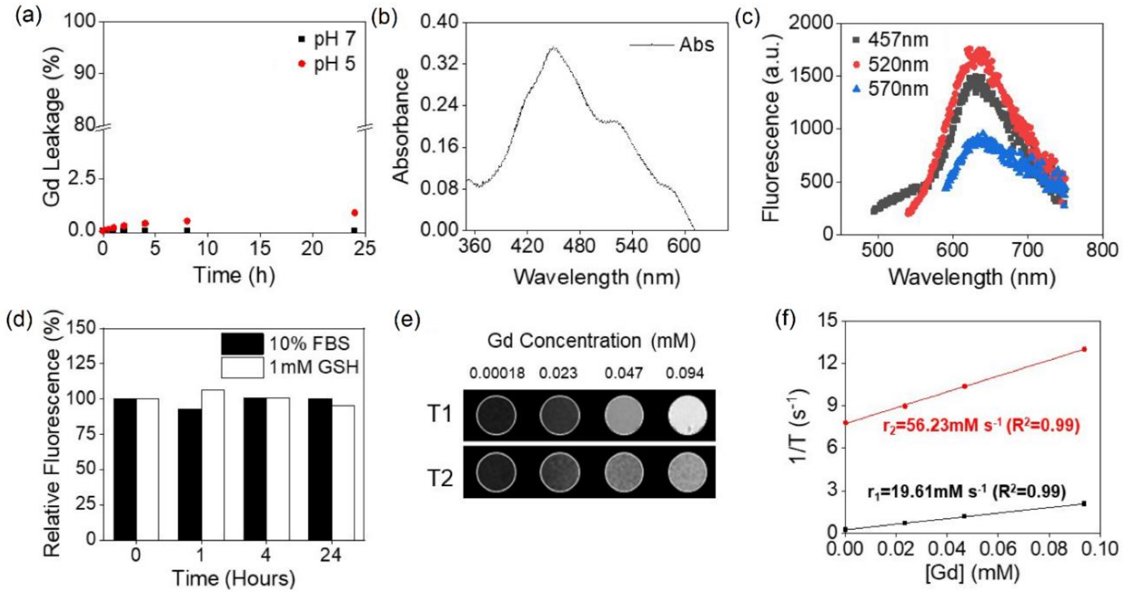

Figure 3.2 Stability, optical properties and magnetic resonance contrast effect of Gd@Cdots (a) Gd^{3+} released from Gd@Cdots in neutral and acidic solution (pH 7 and 5) at 37 ºC for 24 h. The released Gd^{3+} was analyzed using ICP-MS. (b) Absorbance spectrum of Gd@Cdots with peak at 457, 520, and 570 nm. (c) Emission spectra of Gd@Cdots with excitation wavelength at 457, 520, and 570 nm showing the emission peak at 622, 635, and 640 nm, respectively. (d) Fluorescence intensity in various biological environments (10% FBS or 1 mM GSH) for 24 h at 37 ºC showed that Gd@Cdot was stable and not degradable in harsh biological conditions. (e) and (f) MRI phantom experiment using a Varian Magnex 7 Tesla. (e) T1 and T2 MR images of Gd@Cdots (0.00018 - 0.094 mM) in 1% (w/w%) agarose gel. (f) T1 and T2 relaxation of Gd@Cdots evaluated using a quantitative analysis.

Radical production of Gd@Cdots under radiation

We then examined whether Gd@Cdots can enhance radical production under X-ray radiation. This was tested in a Tris buffer solution (pH=7.4) using methylene blue, singlet oxygen sensor green (SOSG), and terephthalic acid (TA) as radical probes. While methylene blue is bleached by a wide range of radicals [29-31], SOSG and TA are flurogenic probes that are selectively responsive to singlet oxygen (O•) and hydroxyl radicals (OH•), respectively [32-35] We found that the presence of Gd@Cdots (30 µg/mL) led to a significantly increased level of methylene blue bleaching under irradiation (5 Gy, Fig. 3.3(a)). Further investigation revealed that both SOSG and TA fluorescence was increased in the presence of Gd@Cdots (Figs. 3.3(b) and (c)). These results indicate that Gd@Cdots can elevate the production of ROS such as O• and OH• under radiation.

For comparison, carbon dots (Cdots) of the same sizes were also prepared and tested. It was found that Cdots also enhanced singlet oxygen (O•) and OH• production, though the level of enhancement was less prominent than Gd@Cdots. This indicates that in addition to high-Z photoelectric effects, the carbon shell may have also played a role in radical generation. We postulate that this enhancement comes from the ability of the Cdots surface to form hydrogen bonds with surrounding water molecules, which would weaken the intramolecular H-OH bond and in turn catalyze water radiolysis. To test this, we repeated TA studies in the presence of Triton X-100, a surfactant that breaks hydrogen bonds, into the solution. Indeed, the addition of the surfactant led to a decreased radical production under radiation, supporting an surface impact on radical production (Fig. 3.3(d)).

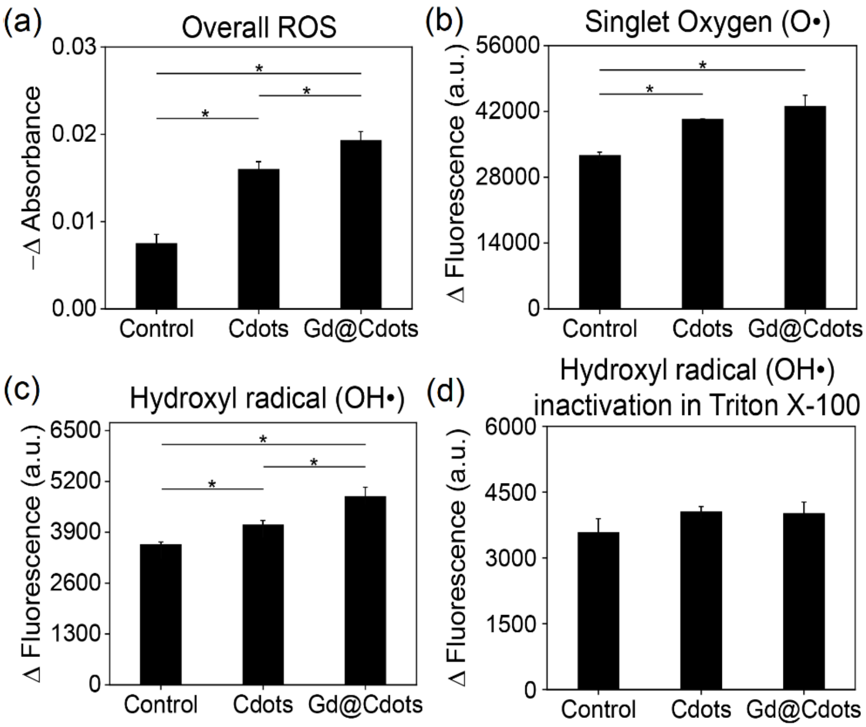

Figure 3.3 Radical production of Gd@Cdots under radiation (a) Overall radical generation of control (H_2O), Cdots (30 µg/mL), and Gd@Cdots (30 µg/mL) evaluated with methylene blue (30 µM) in Tris Buffer (pH 7.4) (n = 4). *$p < 0.05$. (b) Singlet oxygen (O•) generation of control (H_2O), Cdots (30 µg/mL), and Gd@Cdots (30 µg/mL) detected using SOSG (2.5 µM) in Tris Buffer (pH 7.4) (n = 4). *$p < 0.05$. (c) Hydroxyl radical (OH•) generation of control (H_2O), Cdots (30 µg/mL), and Gd@Cdots (30 µg/mL) evaluated with TA (8 mM) in Tris Buffer (n = 4). *$p < 0.05$. (d) Hydroxyl radical production of control (H_2O), Cdots (30µg/mL), and Gd@Cdots (30 µg/mL) after incubation with Triton X-100 using TA (8 mM) in Tris Buffer (n = 4).

In vitro cytotoxicity of Gd@Cdots on H1299 cells

The cytotoxicity of Gd@Cdots in the absence of radiation was tested with H1299 cells using MTT assays. There was no significant particle cytotoxicity even at very high

Gd concentrations (e.g. 1.32 mM, Fig 3.5 (a)). This is in accordance with our previous studies [18-19], and is contributed to minimal metal leakage from the particles. Enhanced radiation damage was assessed by ATP bioluminescence assays. Relative to control cells, Gd@Cdots and radiation (Gd@Cdots+RT, 5 Gy) decreased the cellular ATP level by 36.1% (Fig. 3.5(b)). As a comparison, RT alone caused a 16.3% reduction in intracellular ATP, and Cdots alone under radiation had minimal impact on ATP production (Fig. 3.5(b)).

Given the accumulation of Gd@Cdots in mitochondria, we anticipate that Gd@Cdots would facilitate radiation damage to the organelle. Indeed, compared to radiation alone (5 Gy, the same below), Gd@Cdots+RT led to a drastic decrease of the red-to-green fluorescence ratio in JC-1 staining (from 5.27 to 0.79, Fig. 3.5(c)), which indicates mitochondrial membrane depolarization. This corroborated with cytochrome *c* staining results, which found increased cytochrome *c* release into the cytoplasm when cells were treated with Gd@Cdots plus irradiation (Figs. 3.5(d) and (e)). The released cytochrome *c* would activate intrinsic apoptosis, which was confirmed by caspase 3 assay (Fig. 3.5(f)).

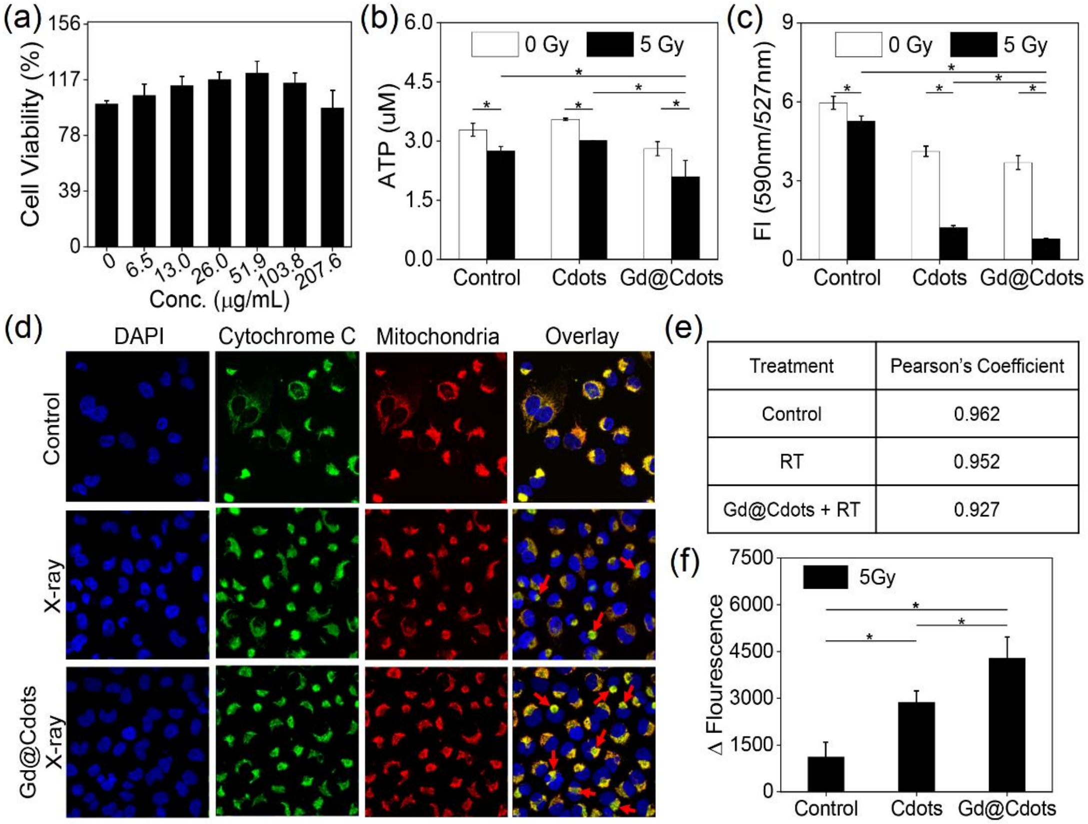

Treatment	Pearson's Coefficient
Control	0.962
RT	0.952
Gd@Cdots + RT	0.927

Figure 3.4 *In vitro* cytotoxicity of Gd@Cdots on H1299 cells (a) Cell viability assessment using MTT assay after 24 h incubation with Gd@Cdots (n = 6). (b) Intracellular ATP evaluation at 24 h after incubation with Gd@Cdots (30 µg/mL), Cdots (30 µg/mL) and H_2O (30 µL/mL) w/o or w/ X-ray irradiation (5 Gy) (n = 4). $^*p < 0.05$. (c) JC-1 assay to evaluate mitochondrial membrane depolarization. H1299 cells were treated for 24 h in the presence of Gd@Cdots (30 µg/mL), Cdots (30 µg/mL) and H_2O (30 µL/mL) w/o or w/ X-ray irradiation (5 Gy) (n = 4). $^*p < 0.05$ on the two way ANOVA. (d) Cytochrome *c* release study after the treatment with Gd@Cdots (30 µg/mL) or control (H_2O, 30 µL/mL) for 4 h under the X-ray radiation at 5 Gy. The released cytochrome *c* into the cytosol was indicated with red arrow. (e) Colocalization analysis using ImageJ to confirm the cytochrome *c* release. (f) Caspase 3 activity after treatment

with Gd@Cdots (30 μg/mL) at 24 h at 5 Gy. Control (H_2O, 30 μL/mL), Cdots (30 μg/mL) were used as comparisons (n = 4). $*p < 0.05$.

Gd@Cdots showed enhanced cytotoxicity under X-ray radiation

Mitochondrion damage would also induce ROS production. This was confirmed by superoxide dismutase (SOD) assay, which found that SOD activity was inhibited by 3.528 U/mL with Gd@Cdots+RT which is significantly large compare to that with Cdots+RT (2.597 U/mL) and RT only (0.314 U/mL) (Fig. 3.6(a)). This SOD inhibition is caused by strong oxidative stress, and it would cause extensive damage to cellular components. Indeed, we found a significantly increased level of lipid peroxidation, manifested in a 49.4% decrease in red-to-green ratio from BODIPY fluorogenic assay (Fig. 3.6(b)). Gd@Cdots also enhanced DNA damage by RT, manifested in a significantly increased level of positive γH2AX staining (Figs. 3.6(c) and S6 in the ESM). It is worth mentioning that some Gd@Cdots were found inside cell nuclei (Fig. 3.4(a)), which may have contributed to DNA damage.

Furthermore, we assessed the dose-modifying effects of Gd@Cdots by clonogenic assay. Briefly, H1299 cells were incubated with Gd@Cdots (10 μg·Gd/mL) or PBS for 12 h and subjected the cells to radiation at elevated doses (0-10 Gy). The treated cells were seeded onto a petri-dish, and after 14 days, colonies with more than 50 cells were counted. The results were fitted into the linear-quadratic equation (Figs. 3.6(d) and (e)). The prescence of Gd@Cdots significantly enhanced the efficacy of RT at all tested doses. The survival fraction at 4 Gy, or SF4, was 0.133 for the Gd@Cdots group, relative to 0.287 in the RT-only control. This represents a nanoparticle-mediated enhanced ratio at 4 Gy, or NER4, of 46.3%. For comparison, gold nanoparticles at the same metal concentration were also tested. Even though Au is a much heavier atom (Z=79, compared to 64 of Gd), gold nanoparticles showed an inferior dose enhancement effect to Gd@Cdots (NER4=0.568, Fig. S7 in the Appendix). It is believed that the enhanced radiosensitizing effects are attributed to Gd@Cdots' unique intracellular distribution pattern and the surface effects.

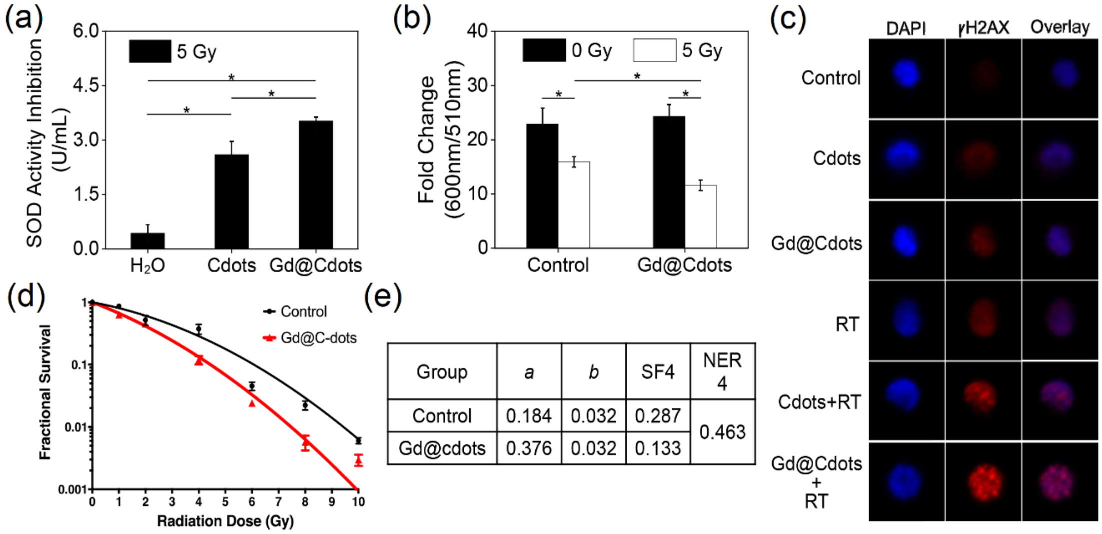

Group	*a*	*b*	SF4	NER 4
Control	0.184	0.032	0.287	0.463
Gd@cdots	0.376	0.032	0.133	

Figure 3.5 Gd@Cdots showed enhanced cytotoxicity under X-ray radiation. (a) SOD activity inhibition of H1299 cells after incubation with H_2O (30 µL/mL), Cdots (30 µg/mL) and Gd@Cdots (30 µg/mL) with X-ray irradiation (5 Gy) (n=3). *$p < 0.05$. (b) Lipid peroxidation of H1299 cells induced by Gd@Cdots w/o or w/ X-ray irradiation (5 Gy) (n = 4). *$p < 0.05$. (c) Representative cell images of rH2AX assay using image stream flow cytometry. H1299 cells were treated for 24 h in the presence of Gd@Cdots (30 µg/mL), Cdots (30 µg/mL) and H_2O (30 µL/mL) w/o or w/ X-ray irradiation (5 Gy). (d) and (e) Clonogenic Assay to evaluate the radio-sensitivity of H1299 cells after treatment with Gd@Cdots. (d) Clonogenic assary results, tested in H1299 cells at different doses. Control group received radiation only. (e) Survival (S) as a function of

radiation dose (D) was fitted into the linear-quadratic formula $S(D)/S(0)=\exp-(aD+bD^2)$.

***In vivo* studies of Gd@Cdots on tumor targeting, host clearance and tumor therapy**

We then tested Gd@Cdots *in vivo*. Briefly, we subcutaneously inoculated H1299 tumors onto the right flank of nude mice. When the tumor size reached ~500 mm^3, Gd@Cdots were i.v. injected. The animals were scanned on a 7T MRI at different time points. There was a significant increase of signals in tumor areas, indicating particle accumulation in tumors through the EPR effect (Fig. 3.7(a)), which we observed in our previous studies.[18] ROI analysis showed that the signal-to-background ratio (SNR) was elevated in the first 6 h, and was dropped to the background level at 72 h (Fig. 3.7(a)).

Therapy studies were also conducted in H1299 tumor bearing mice. The animals were randomly divided to receive treatments including Gd@Cdots plus radiation (Gd@Cdots+RT), radiation only (RT), and PBS (n=5). For the Gd@Cdots+RT group, Gd@Cdots at 0.1 mmol·Gd/kg were i.v. injected; 6 Gy was delivered via a single beam to tumors at 4 h, with the rest of the body shielded by lead. The same radiation dose was applied to the RT only group. Adding Gd@Cdots to the regimen significantly improved RT outcomes, leading to a tumor inhibition rate (TIR) of 80.3% on Day 30 relative to PBS control (Fig. 3.7(b)). By the end of our study (Day 48), 80% of the animals in the Gd@Cdots+RT group remained alive (Fig. 3.7(c)). In contrast, RT only group caused mediocre tumor suppression, showing a TIR of 37.2% on Day 30 (Fig. 3.7(b)) and an animal survival of 42 days (Fig. 3.7(c)). After therapy studies, tumor tissues were collected, and histology analysis was performed (Fig. 3.7(d)). H&E and TUNEL staining found that Gd@Cdots+RT led to an elevated level of apoptosis and a reduced level of cell density in tumors. These results corroborate with the tumor growth trend and animal survival data (Figs. 3.7(b) and (c)), validating the radiosensitizing effects by Gd@Cdots.

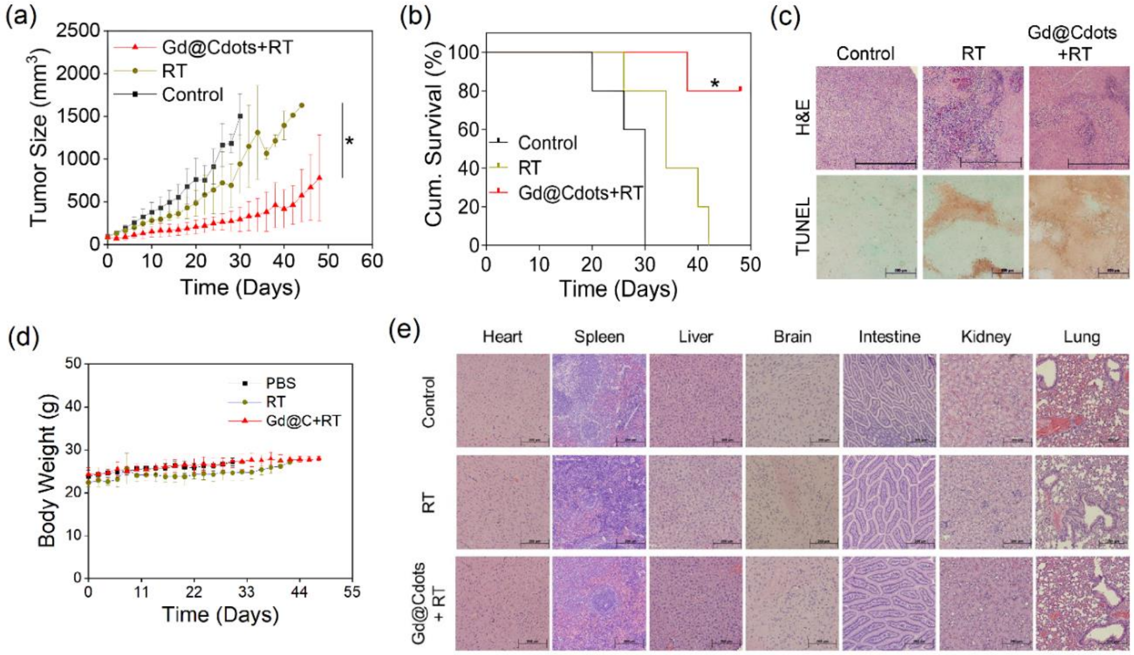

Figure 3.6 *In vivo* studies of Gd@Cdots (a) Tumor growth curve of H1299 tumor bearing mice (n = 5) after treatment. Gd@Cdots or PBS were intravenously injected and followed by X-ray radiation at 6 Gy. PBS treatment only without using radiation was used as a control (n=5). *$p < 0.05$ compare to control and RT groups. (b) Survival curve of H1299 tumor bearing mice after treatment (n=5). *$p < 0.05$ compare to control and RT groups on Mantel-Cox test. (c) Representative images of H&E Staining (scale bars, 500 μm) and TUNEL assay (scale bars, 500 μm) on H1299 tumors after intravenous injection with Gd@Cdots or PBS followed by X-ray radiation at 6 Gy. PBS treatment only without using radiation was used as a control. The brown staining of TUNEL assay indicates an apoptotic cell death whereas the blue staining is counterstaining. (d) Body weight observation during the therapy study (e) H&E staining of the major tissues.

Meanwhile, there was no significant animal body weight drop throughout the entire therapy study (Fig S8(a)). After euthanizing the animals, the major organs were collected and analyzed. H&E staining found no sign of toxicity in all tested organs, including the heart, spleen, liver, brain, intestine, kidney, and lung (Fig. S8(b) in the ESM). To further assess nanoparticle toxicity, in a separate study, Gd@Cdots (0.1 mmol/kg) were injected into healthy mice, and blood samples were collected for analysis on Day 14. Complete blood count (CBC) found no significant difference between Gd@Cdots and PBS control groups in all tested indices (Table S1 in the ESM). BUN and ALT levels were also in the normal ranges (Table S1 in the ESM). Overall, while improving RT damage to tumors, Gd@Cdots caused little systemic toxicity.

HZNPs as an emerging type of radiosensitizer have attracted a lot of recent attention. Despite initial concerns about the relatively low X-ray cross-section of high-Z elements at high-energy beams, a number of studies have demonstrated improved RT efficacy with gold, hafnium oxide, and gadolinium nanoparticles in both pre-clinical and clinical settings.[1, 38-41] However, HZNPs are often associated with issues such as slow clearance and toxicity. Specifically, conventional nanoparticles are often ~20-200 nm in diameter and after i.v. injection they are largely accumulated in the reticuloendothelial system (RES) organs such as the liver and spleen, and/or stuck in the microvessels of normal lung tissues. This is problematic because radiation planning does not take these nanoparticles into account. Meanwhile, many HZNPs while temporally stable, are gradually decomposed inside hosts to release toxic heavy metals. Our Gd@Cdots are advantageous in this context for they are efficiently excreted through renal clearance due to their ultrasmall sizes and minimally releasing heavy metals owing to carbon protection.

Moreover, unlike conventional HZNPs that are often single-component metals or metal oxides, Gd@Cdots are a composite material. This is a benefit from the perspective of nanoparticle engineering because now the photoelectric effects and surface effects rely on two different components (high-Z dopants and carbon shell, respectively), each of which can be potentially adjusted with flexibility. For instance, it is possible to load other metals, including heavier ones such as Eu and Bi, into the carbon shell. It is also possible to change carbon precursors, which may yield Gd@Cdots of varied shell compositions and surface properties. These changes may alter cellular uptake, biodistribution, and radiosensitizing effects of Gd@Cdots and potentially enhance the efficacy of RT further.

3.4 Conclusions

Overall, several factors contribute to the radiosensitizing effects of Gd@Cdots. In addition to high-Z photoelectric effects, surface-catalyzed radical production also seems to plays a role. Moreover, due to the positive surface charge and ultrasmall sizes, nanoparticles can enter cells and accumulate in mitochondria and even cell nucleus. Such intracellular distribution facilitates radiation damage to these critical organelles. In the current study, we exploited nanoparticles’ small sizes and tumor EPR effect to achieve tumor accumulation. It is feasible to couple a tumor targeting ligand to Gd@Cdots, which may improve cancer cell targeting and internalization. The related studies are underway.

CHAPTER 4

HIGH-Z METAL LOADED CARBON NAOPARTICLES AND *IN VIVO* IMAGING : TUMOR TARGETING, CLEARENCE, AND TOXICITY STUDES [3]

---

[3] Hongmin Chen, Yuwei Qiu, Dandan Ding, Huirong Lin, Wenjing Sun, Geoffrey D. Wang, Weicheng Huang, Weizhong Zhang, Daye Lee, Gang Liu, Jin Xie, Xiaoyuan Chen. Adv. Mater. 2018, 30, 1802748.

Reprinted here with permission of the publisher.

ABSTRACT

Near-infrared (NIR) range from 650 to 950 nm is called the first therapeutic window and widely used for pre-clinical in vivo and tissue imaging. The conventional small organic dyes and semiconductor quantum dots (QDs) are limited their application due to photostability and toxicity, respectively. Carbon dots (CDs) have been considered as a potential optical imaging probs due to their unique fluorescent nature, high photobleaching resistivity, low cytotoxicity, and good aqueous solubility. However, since most CDs have broad absorption peaks in the UV-vis (230-280 nm) with blue to green emission, CDs with strong red fluorescence is still desired. In the previous chapters, both Gd@Cdots and Bi@Cdots synthesized with p-phenylenediamine (pPD) showed strong red fluorescence at 623 nm and 635 nm respectively. Therefore, these particles may have potential as a fluorescence imaging contrast agent. Moreover, depending on the metals loaded in the particles, the M@Cdots can be used as an imaging contrast agent for other imaging tools.

4.1 Introduction

In vivo imaging is one of the essential tools for diagnosis or monitor the progression of disease in cancer research, and optical imaging is an imaging technique which uses lights to get structural information on tissues, organs, cells, and molecules. Optical imaging brings benefits over other imaging tools in terms of safety because it does not require any harmful ionizing radiation such as x-ray.[1-3] Instead, it uses non-ionizing radiation such as visible, ultraviolet, and infrared lights. [1-5] Therefore, optical imaging can be used over and over without causing any side effects. [1-3]

Near-infrared (NIR) range from 650 to 950 nm is called the first therapeutic window and widely used for pre-clinical in vivo and tissue imaging due to low autofluorescence resulting in deeper tissue penetration.[6-8] Many small organic dyes such as cyanine and rhodamine have been proposed for NIR imaging, but they have poor photostability resulting in short lifetime.[8] Semiconductor quantum dots (QDs) can be another candidate for fluorescence imaging contrast agent with high quantum yield and tunable fluorescence.[9-11] However, their heavy metal contents such as cadmium can be potentially toxic, and this limits application in bioimaging.[12-14] Therefore, NIR fluorescence imaging contrast agents with low toxicity, long lifetime, and high quantum yield are still desired.

Carbon dots (CDs) have been considered as a potential optical imaging probs due to their unique fluorescent nature, high photobleaching resistivity, low cytotoxicity, and good aqueous solubility.[15-17] Many studies have presented CDs synthesized with different methods and carbon sources. [18-22] However, most CDs have broad absorption peaks in the UV-vis (230-280 nm) with blue to green emission which is not suitable for deep tissue imaging. [18, 19] Therefore, create CDs with strong red fluorescence is challenge. Recent studies showed that the surface groups or dopants on the CDs are strongly related to the absorption and emission spectrum.[15, 23] For example, if there are more nitrogen doping, the absorption and emission peak will be shifted to higher wavelength with stronger quantum yield.[20, 23]

The carbon precursor p-phenylenediamine has two amine groups on the para position of benzene ring which result in large amount of nitrogen doping on the carbon shell. As a result, both Gd@Cdots and Bi@Cdots showed strong red fluorescence at 624 nm and 633 nm respectively. Therefore, these particles may be useful for tracking the particle accumulation, distribution, and clearance *in vivo*. Moreover, with the metals, loaded in the particles, the M@Cdots can be used as an imaging contrast agent for other imaging tools. For example, Gd is a T1 contrast agent for magnetic resonance imaging (MRI), and Bi is computed tomography (CT) contrast agent. Therefore, Gd@Cdots and Bi@Cdots can be a potential MRI and CT contrast agent, respectively.

On this chapter, optical properties of Gd@Cdots were explored as a fluorescence imaging agent as well as an MRI contrast agent. The particles showed the strong red fluorescence at 580nm with good photostability. Moreover, they showed high r_1 relaxivity ($16.0 \times 10^{-3}\ \mathrm{M}^{-1}\ \mathrm{s}^{-1}$) and low r_2 relaxivity ($23.8 \times 10^{-3}\ \mathrm{M}^{-1}\ \mathrm{s}^{-1}$) suggesting a low r_2/r_1 and great potential of Gd@Cdots as a T_1 contrast agent. With these promising data, we investigated the particle accumulation in tumor and clearance *in vivo*. The result showed that the ultra-small Gd@Cdots are cleared out by renal clearance within a short period time suggesting minimal in vivo toxicity. We confirmed the toxicity of the particles by blood and serum test.

4.2 Material and method

Materials

p-Phenylenediamine (pPD) (Sigma Aldrich, Cat# 78429), Gadolinium nitrate hexahydrate (Gd(NO3)3•6H2O, Sigma Aldrich, Cat# 211591), Ethanol (KOPTEC, Cat# 19J14D), Dialysis membrane (Spectrum, [MWCO]=100-500), Milli-Q H2O, 3-(4,5-Dimethylthiazolyl-2)-2,5-diphenyltetrazolium bromide (MTT) (Sigma Aldrich, Cat# M2128).

Gd@Cdots Synthesis

Gd@Cdots were synthesized by a hydrothermal method. Briefly, 0.16g of pPD and 0.6g of $Gd(NO_3)_3$ were dissolved in 60 mL EtOH, and the solution was transferred into a 100 ml poly(tetrafluoroethylene)-lined stainless steel autoclave. The reaction was heated at 180 °C for 12 h and cooled down to room temperature. The obtained dark red suspension was purified using dialysis membrane (MWCO 500) against to Milli-Q water for 17 h to remove bi-carbon products and extra Gd^{3+} free ions. The final product was freeze dried for further experiment and long-term storage.

Absorbance and fluorescence

The UV-Vis absorbance spectra were obtained on a BioTek Synergy MX multi-mode microplate reader and the PL emission and excitation spectra were acquired on a Hitachi F-7000 spectrophotometer under ambient conditions.

MRI phantom Study

MRI phantom studies. The Gd@GCNs with elevated concentrations (0-0.025 mM) were suspended in 200 µl PCR tubes and the MR imaging measurements were performed on a 7T 3 Varian small animal MRI system. For the T1-weighted MR images, a T1 inversion recovery fast spin echo (FSE) sequence was used based on the following parameters: TR = 5000 ms, TE = 12 ms, ETL = 8, inversion times (TI) = 5, 10, 30, 50, 80, 200, 500, 700, 900, 1200 and 3000 ms. As for the T2-weighted MR images, a FSE sequence was used according to the following parameters: TR = 3 s, TE=10, 20, 30, 40, 50, 60, 70, 80, 90 and 100 ms. 256×256 matrices.

Physical stability and photo-stability of Gd@GCNs. The Gd@GCNs were incubated different pH (3-11) and the fluorescence intensity over time was monitored under excitation of 350 nm, 420 nm and 500 nm, respectively. In the photo-stability study, the Gd@GCNs and CdSe@ZnS quantum dots with the same emission intensity (500 nm excitation) were irradiated continuously with UV lamps (254 nm, 6W) for 5-30 min and the fluorescence was monitored.

In vivo fluorescence imaging

The animal studies were performed according to the protocol approved by the Institutional Animal Care and Use Committee (IACUC) of University of Georgia. In the in vivo fluorescent imaging experiments, the 4-6 weeks athymic nude mice (Harlan) (18-20 g) received a subcutaneous injection of 5 µl (4 mg/mL) of Gd@GCNs. The excitation wavelength was 500-750 nm with a step of 50 nm and the collected emission channels were 510-900 nm. The exposure time was 0.5 s. Before in vivo tumor targeting imaging, the SCC-7 tumor model was developed by subcutaneous injection of 1×106 cells into the right front flank of female athymic nude mice (Harlan Laboratories). In the fluorescent biodistribution study, 200 µl of the Gd@GCNs were injected into the SCC-7 bearing mice (0.1 mmol/kg, Gd, n=3). The images were taken on a 6 Maestro II imaging system

(PerkinElmer) at 10 min, 30 min, 1 h, 3 h, and 24 h post injection (p.i.). The urine was imaged and collected for ex vivo fluorescence analysis.

In vivo MRI study

The H1299 tumor bearing nude mice (n=3) was investigated using a Varian 7T magnet. When the tumor size reached 500 mm^3, Gd@Cdots (0.1 mmol/kg based on Gd) was intravenously injected. Transverse and coronal T1-weighted MR images were obtained at 0.5, 1, 2, 4, 6, and 72 h using following sequences: field-of-view (FOV) = 70×70 mm^2, TR/TE = 500/12 ms, matrix size = 256×256, slice = 4. Thickness = 1 mm. The signal to background was evaluated using ImageJ software.

Hematology and Serum Chemistry

In a separated experiment, three balb/c mice were intravenously injected with PBS or Gd@Cdots (0.1 mmol Gd/kg). Blood samples were collected using a cardiac puncture blood collection method. 250 µL of each blood samples were tested for a complete blood count to evaluate the number of each type of blood cells. Remaining blood samples were used to evaluate liver and kidney function using Alanine Aminotransferase (ALT) ELISA kit (Abcam, Cat# ab105134) and Urea Nitrogen (BUN) detection kit (Arbor Assays, Cat# K024H1).

4.3 Result and discussion

Optical properties and magnetic resonance contrast effect of Gd@Cdots

we investigated the optical properties of Gd@Cdots. UV–vis analysis found three peaks at 465, 526, and 710 nm, suggesting the existence of multiple electronic transitions (Fig 4.1a).[24] As a comparison, conventional Cdots and Gd@Cdots showed only one broad peak in the UV region that corresponded to a $\pi \rightarrow \pi^*$ transition. Moreover, Gd@Cdots displayed strong red fluorescence, whereas conventional Cdots showed weak luminescence above 550 nm (Fig 4.1b).[25, 26] A closer examination found multiple emission peaks at 550, 570, and 580 nm, which were derived from excitations at 400, 520, and 550 nm, respectively (Fig. 4.1b). The maximum quantum yield was 10.2% under excitation at 550 nm.

We also studied the impact of pH and long-term light exposure on the luminescence properties of Gd@Cdots. As shown in Fig 4.1c, changing the pH from 3 to 10 did not affect the nanoparticles' fluorescence. Irradiation with 254 nm UV light for 0.5 h did not bleach the nanoparticles either (Fig 4.1d, e). As a comparison, the fluorescence of commercial CdSe@ZnS quantum dots (QDs) was completely bleached within 30 min. These data suggested the superior chemical and photostability of the nanoparticles.[27]

We measured the longitudinal (r_1) and transverse (r_2) relaxivities of Gd@Cdots through an agar gel phantom study on a Varian 7.0 T imaging system (Fig. 4.1f, g). The r_1 relaxivity of Gd@Cdots was $16.0 \times 10^{-3}\ \mathrm{M}^{-1}\ \mathrm{s}^{-1}$ (Fig 4.1g), which was more than five times higher than that of Gd-DTPA ($3.1 \times 10^{-3}\ \mathrm{M}^{-1}\ \mathrm{s}^{-1}$) on the same Gd basis.[28] The r_2 relaxivity was $23.8 \times 10^{-3}\ \mathrm{M}^{-1}\ \mathrm{s}^{-1}$, suggesting a low r_2/r_1 and great potential of Gd@Cdots as a T_1 contrast agent.

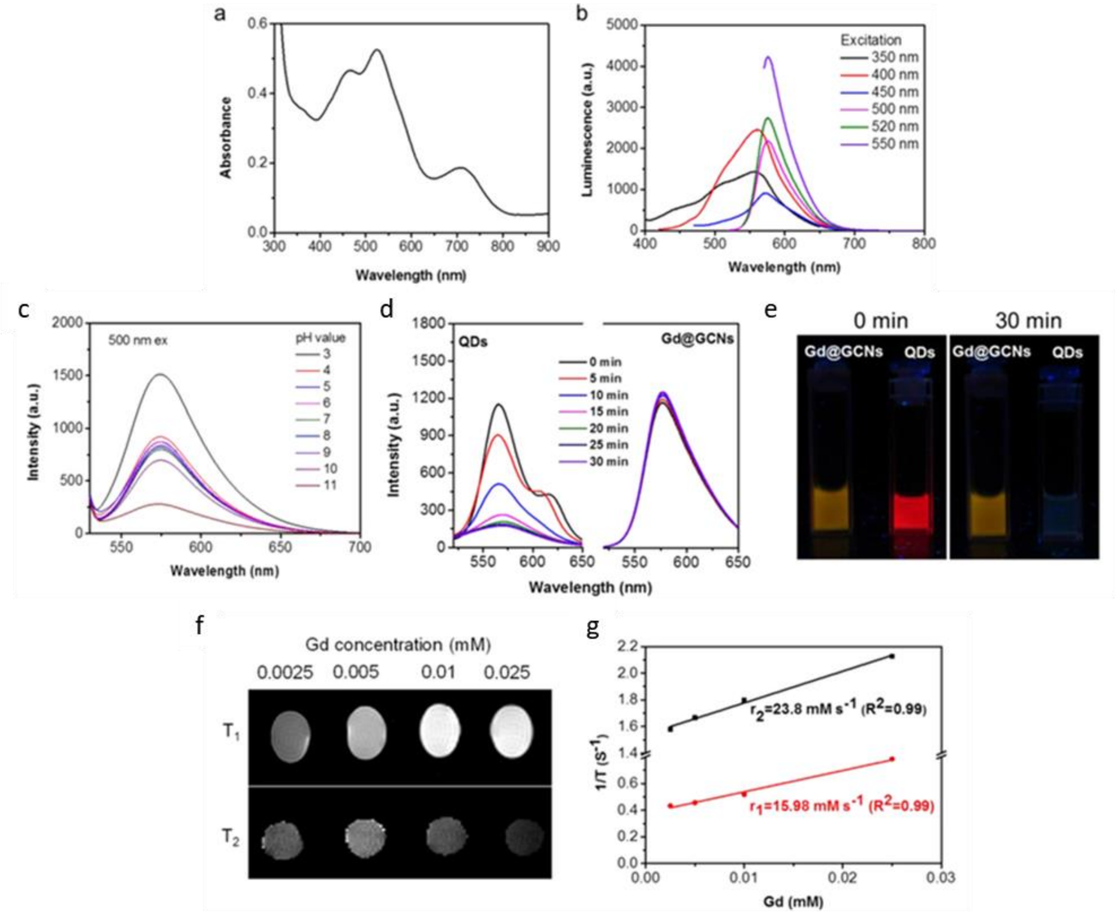

Figure 4.1 Optical properties and magnetic resonance contrast effect of Gd@Cdots

a. Absorption spectrum of the Gd@Cdots b. Emission spectra of the Gd@Cdots c. Stability of Gd@Cdots in different pH solutions for 24h. d. Photostability of the Gd@Cdots under 253 nm UV light (8W) irradiation. Compared with commercial CdSe@ZnS QDs, the Gd@Cdots showed excellent photostability. The CdSe/ZnS QDs showed rapid photobleaching due to the light-irradiated surface redox reaction. (e) Comparison of the photostability of the Gd@Cdots in water and CdSe/ZnS QDs in chloroform. The solutions were under continuous irradiation with UV light (8 W, 254 nm) for different durations of time. (f) T_1 and T_2 MR images of the Gd@Cdots in 1 wt% agarose gel of the 7 T system. The upper part in the panel shows the T_1 images and the lower part shows the T_2 images.

(g) R_1 and R_2 relaxivities of the Gd@Cdots as a function of the molar concentration of Gd^{3+} in the solution.

In vivo imaging studies

Next, we explored the feasibility of using Gd@Cdots as a fluorescence and MRI dual modal imaging probe in vivo. We started by subcutaneous injection of 5 and 20 μL of 2 mg mL^{-1} Gd@Cdots to the back of a nude mouse. We then scanned the mouse in a Maestro system. We observed strong red fluorescence at the injection site. The signals can be clearly differentiated from the autofluorescence from the animal body (4.2a). For fluorescence imaging, we injected Gd@Cdots (0.1 mmol Gd kg^{-1}) via the tail vein to the SCC-7 tumor-bearing nude mice ($n = 3$) and then scanned the animals on a Maestro II system at 10, 30 min, 1, 3, and 24 h post-injection (Fig. 4.2b). Strong fluorescence signals were found in the tumor region, and the intensity peaked at 1 h. This result was attributed to the EPR effect–mediated nanoparticle deposition in tumors. For *in vivo* MRI study, we intravenously injected Gd@Cdots (0.1 mmol Gd kg^{-1}) to the H1299 tumor-bearing nude mice and obtained T_1-weighted images using 7T 3 Varian small animal MRI system (Fig 4.2c). The result showed that the Gd@Cdots can efficiently accumulate in tumor without any targeting ligand. The signal to background ratio suggested that the highest particle accumulation can be reached at 1 h post-injection which agreed with the fluorescence imaging results (Fig 4.2d).

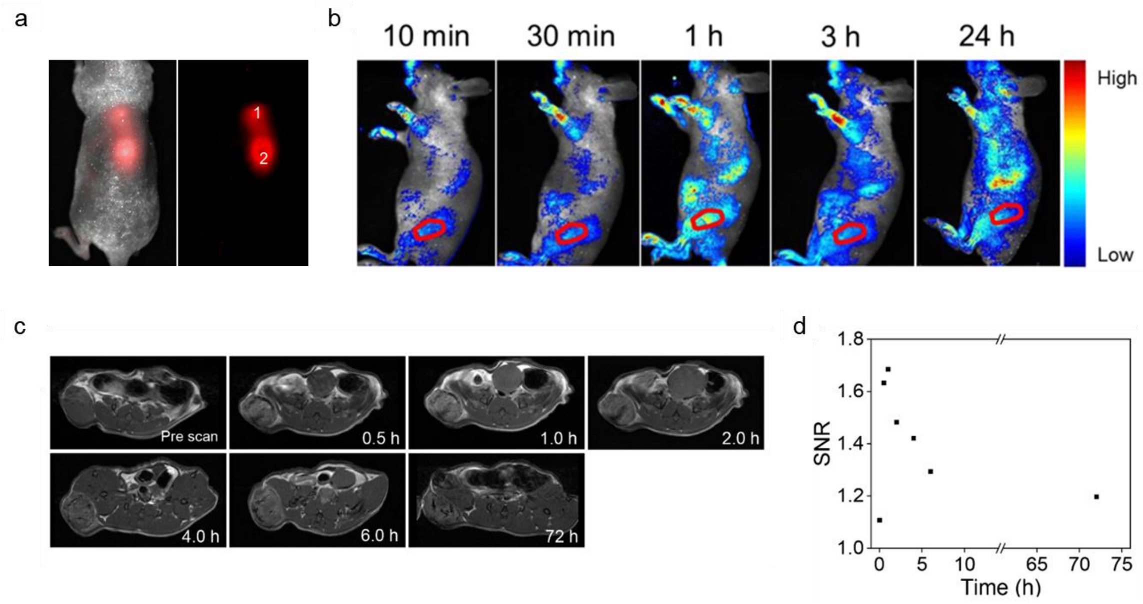

Figure 4.2 In vivo imaging studies a. *In vivo* fluorescence images after subcutaneous injection of Gd@GCNs (1 mg/mL) into different areas (Excitation**:** 500 nm; Emission: 520-750 nm). Injection: 10 µL (area 1) and 30 µL (area 2). b. *In vivo* fluorescence images from nude mice bearing tumors after intravenous injection of Gd@Cdots at different time intervals. Ex: 500nm, Em: 520-720 nm. The red circles mark the tumor position. c. T_1-weighted MRI images, taken at different time points after Gd@Cdots injection (0.1 mmol Gd/kg). d. Signal-to-background ratios (SNRs) based on the imaging results.

Particle tumor targeting, clearance, and in vivo toxicity studies

Interestingly, intense fluorescence signals were found in the bladder after the nanoparticle injection (Fig 4.3a), suggesting renal clearance of the nanoparticles. To examine the integrity of the nanoparticles after excretion, we collected urine samples after 0.5 h and subjected them to centrifugal filtration (MWCO = 3000). We observed strong fluorescence characteristic of Gd@Cdots in the upper fraction. (Fig 4.3b) Meanwhile, no fluorescence was found in the filtrate. This result was also confirmed by TEM, as intact Gd@Cdots were found in the upper fraction but none were found in the filtrate. (Fig 4.3c) For in vivo MRI, we intravenously injected Gd@Cdots (0.1 mmol Gd kg^{-1}) into nude mice and scanned the animals at 0.5, 1, 3, and 24 h on a 7 T system. We also found hyperintensities in the bladder at 30 min after nanoparticle injection (Fig 4.3d, e), confirming efficient renal clearance.

For assessment of toxicity, in a separate study, Gd@Cdots (0.1 mmol/kg) were injected into healthy mice, and blood samples were collected on Day 14 for analysis. Complete blood count (CBC) and biochemistry analyses found no significant difference between the Gd@Cdots and PBS groups in all tested indices. (Table 4.1) BUN and ALT levels were also in the normal ranges, confirming low toxicity. (Table 4.1)

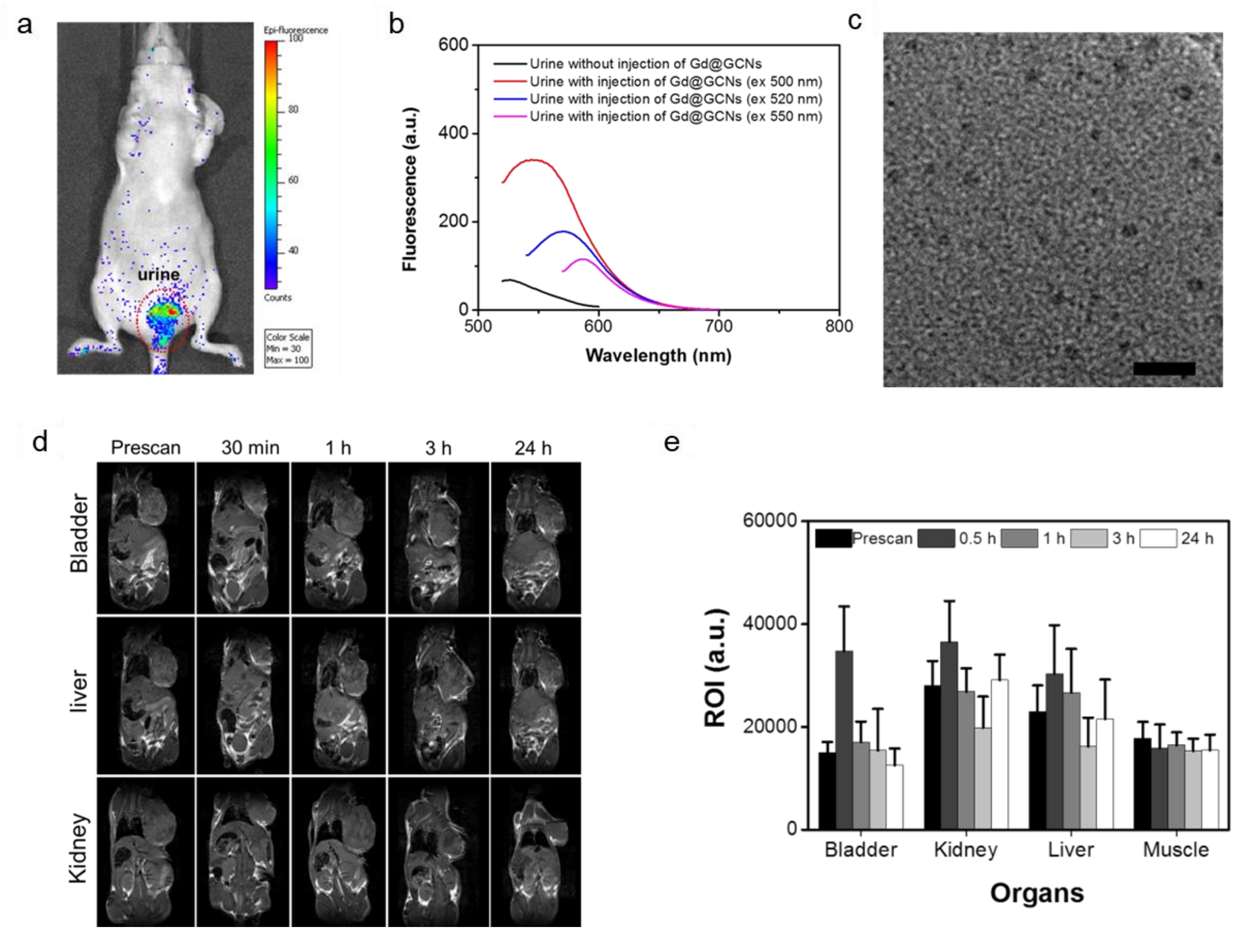

Figure 4.3 Particle clearance study a. Representative *in vivo* fluorescence image of the bladder area after i.v. injection of Gd@Cdots at 30 min (ex: 500 nm. Em: filter dsRED). b. Fluorescent analysis of the urine samples obtained from the mice with and without injection of Gd@Cdots. c. TEM image of the fragments after purification of urines (scale bar: 20 nm). d. T_1-weighted MR images acquired at different time points after injection of the Gd@Cdots. e. Signal change in the bladder, liver, and kidney based on the analysis of the images in a.

Table 4.1. Complete blood count (CBC) results and liver & kidney function tests (0.1 mmol Gd/Kg).

	Unit	Reference (95% interval)		Experiment			
				Control		Gd@Cdot	
		Low	High	Average	Std	Average	Std
RBC	x 10^6/ul	8.16	11.69	11.75	0.21	11.10	0.26
HGB	g/dl	12.40	18.90	18.50	0.14	17.30	0.61
HCT	%	43.50	67.00	54.60	1.84	52.67	2.06
MCV	fl	50.80	64.10	46.60	0.85	47.57	0.67
MCH	pg	13.00	17.60	15.75	0.07	15.63	0.47
MCHC	g/dl	23.90	33.10	33.85	0.78	32.40	1.27
RDW	%	16.90	23.50	13.75	0.35	14.10	0.17
Platelets	x10^3/ul	476.00	1661.0	229.50	94.05	538.67	250.23
MPV	fl	4.60	5.80	5.55	0.49	6.17	0.15
WBC	x10^3/ul	5.69	14.84	6.00	1.41	7.03	0.45
Neutrophils	x10^3/ul	0.74	3.01	1.27	0.11	1.38	0.41
Lymphocytes	x10^3/ul	3.60	11.56	4.03	1.24	5.18	0.56
Monocytes	x10^3/ul	3.75	14.33	0.10	0.06	0.23	0.07
Eosinophils	x10^3/ul	0.01	0.35	0.34	0.41	0.12	0.05
Basophils	x10^3/ul	0.00	0.16	0.27	0.18	0.12	0.04
BUN	mg/dL	7.00	31.00	24.39	4.19	21.17	3.71
ALT	unit/L	40.00	170.00	58.29	3.63	54.10	1.50

3.4 Conclusion

Gd@C-dots afford good r_1 relaxivity and strong photoluminescence, making them appealing MRI/fluorescence dually functional imaging probes. This potential is strengthened by the fact that Gd@Cdots and their conjugates can be efficiently excreted through renal clearance after systematic injection. Our observations suggest great potential of Gd@Cdots in clinical translation as safe and efficient imaging probes.

CHAPTER 5

CONCLUSIONS AND FUTURE WORK

HZNPs as an emerging type of radiosensitizer have attracted a lot of recent attention. Despite initial concerns about the relatively low X-ray cross-section of high-Z elements at high-energy beams, a number of studies have demonstrated improved RT efficacy with gold, hafnium oxide, and gadolinium nanoparticles in both pre-clinical and clinical settings. However, HZNPs are often associated with issues such as slow clearance and toxicity. Specifically, conventional nanoparticles are often ~20-200 nm in diameter and after i.v. injection they are largely accumulated in the reticuloendothelial system (RES) organs such as the liver and spleen, and/or stuck in the microvessels of normal lung tissues. This is problematic because radiation planning does not take these nanoparticles into account. Meanwhile, many HZNPs while temporally stable, are gradually decomposed inside hosts to release toxic heavy metals. Our Gd@Cdots are advantageous in this context for they are efficiently excreted through renal clearance due to their ultrasmall sizes and minimally releasing heavy metals owing to carbon protection.

Moreover, unlike conventional HZNPs that are often single-component metals or metal oxides, M@Cdots are a composite material. This is a benefit from the perspective of nanoparticle engineering because now the photoelectric effects and surface effects rely on two different components (high-Z dopants and carbon shell, respectively), each of which can be potentially adjusted with flexibility. For instance, as I presented on chapter 2, it is possible to load different metals such as Bi into the carbon shell. Moreover, particle can be prepared with various carbon precursors including pPD, ABA, and CA which can result in varied shell compositions and surface properties on M@Cdots. The preliminary study showed that the particle prepared to different composition affect to radiosenstizing effect. Therefore, in the future study, we will explore the efficacy of RT by different M@Cdots synthesized with various metals and carbon sources.

REFERENCES

CHAPTER 1:

1. Bray, F., et al., *Global cancer statistics 2018: GLOBOCAN estimates of incidence and mortality worldwide for 36 cancers in 185 countries.* CA: A Cancer Journal for Clinicians, 2018. **68**.
2. Anand, P., et al., *Cancer is a Preventable Disease that Requires Major Lifestyle Changes.* Pharmaceutical Research, 2008. **25**(9): p. 2097-2116.
3. Jayasekara, H., et al., *Long-Term Alcohol Consumption and Breast, Upper Aero-Digestive Tract and Colorectal Cancer Risk: A Systematic Review and Meta-Analysis.* Alcohol and Alcoholism, 2015. **51**(3): p. 315-330.
4. Lee, K.H., et al., *Is rigid fixation of the greater trochanter necessary for arthroplasty of intertrochanteric fractures?* Orthopaedics & Traumatology: Surgery & Research, 2019. **105**(1): p. 41-45.
5. Mirabello, L., R.J. Troisi, and S.A. Savage, *Osteosarcoma incidence and survival rates from 1973 to 2004: data from the Surveillance, Epidemiology, and End Results Program.* Cancer, 2009. **115**(7): p. 1531-1543.
6. Wancata, L.M., et al., *Conditional survival in advanced colorectal cancer and surgery.* The Journal of surgical research, 2016. **201**(1): p. 196-201.
7. Pollack, L.A., et al., *Introduction: charting the landscape of cancer survivors' health-related outcomes and care.* Cancer, 2009. **115**(18 Suppl): p. 4265-9.

8. Lederman, M., *The early history of radiotherapy: 1895–1939.* International Journal of Radiation Oncology, Biology, Physics, 1981. **7**(5): p. 639-648.

9. Grubbé, E.H., *Priority in the Therapeutic Use of X-rays.* Radiology, 1933. **21**(2): p. 156-162.

10. Connell, P.P. and S. Hellman, *Advances in Radiotherapy and Implications for the Next Century: A Historical Perspective.* Cancer Research, 2009. **69**(2): p. 383-392.

11. Jean-Claude, R. and F. Nüsslin, *Marie Curie's contribution to Medical Physics.* Physica Medica: European Journal of Medical Physics, 2013. **29**(5): p. 423-425.

12. WickhamLouis and Degrais, *Radium - Thérapie.* Archives of The Roentgen Ray, 1909. **14**(4): p. 127-128.

13. Boone, M.L.M., et al., *Introduction to the use of protons and heavy ions in radiation therapy: Historical perspective.* International Journal of Radiation Oncology*Biology*Physics, 1977. **3**: p. 65-69.

14. Fry, D.W., et al., *A Travelling-Wave Linear Accelerator for 4-MeV. Electrons.* Nature, 1948. **162**(4126): p. 859-861.

15. Altorki, N. and S. Harrison, *What is the role of neoadjuvant chemotherapy, radiation, and adjuvant treatment in resectable esophageal cancer?* Annals of cardiothoracic surgery, 2017. **6**(2): p. 167-174.

16. Begg, A.C., F.A. Stewart, and C. Vens, *Strategies to improve radiotherapy with targeted drugs.* Nature Reviews Cancer, 2011. **11**(4): p. 239-253.

17. Jain, V. and A.T. Berman, *Radiation Pneumonitis: Old Problem, New Tricks.* Cancers (Basel), 2018. **10**(7).

18. Furdui, C.M., *Ionizing radiation: mechanisms and therapeutics.* Antioxidants & redox signaling, 2014. **21**(2): p. 218-220.

19. Banerjee, R. and M. Kamrava, *Brachytherapy in the treatment of cervical cancer: a review.* International journal of women's health, 2014. **6**: p. 555-564.

20. Schwarz, S.B., et al., *Iodine-125 brachytherapy for brain tumours - a review.* Radiation Oncology, 2012. **7**(1): p. 30.

21. Parashar, B., et al., *Cesium-131 permanent seed brachytherapy: Dosimetric evaluation and radiation exposure to surgeons, radiation oncologists, and staff.* Brachytherapy, 2011. **10**(6): p. 508-513.

22. Tantivatana, T. and K. Rongsriyam, *Treatment outcomes of high-dose-rate intracavitary brachytherapy for cervical cancer: a comparison of Ir-192 versus Co-60 sources.* J Gynecol Oncol, 2018. **29**(5).

23. Nohara, T., et al., *Clinical Results of Iridium-192 High Dose Rate Brachytherapy with External Beam Radiotherapy.* Japanese Journal of Clinical Oncology, 2010. **40**(7): p. 677-683.

24. Skowronek, J., *Current status of brachytherapy in cancer treatment - short overview.* Journal of contemporary brachytherapy, 2017. **9**(6): p. 581-589.

25. Frassica, D.A., *General principles of external beam radiation therapy for skeletal metastases.* Clin Orthop Relat Res, 2003(415 Suppl): p. S158-64.

26. Sadeghi, M., M. Enferadi, and A. Shirazi, *External and internal radiation therapy: Past and future directions.* Journal of Cancer Research and Therapeutics, 2010. **6**(3): p. 239-248.

27. Cook, A.M. and R.J. Berry, *Direct and Indirect Effects of Radiation : their Relation to Growth.* Nature, 1966. **210**(5033): p. 324-325.

28. Alizadeh, E., T.M. Orlando, and L. Sanche, *Biomolecular Damage Induced by Ionizing Radiation: The Direct and Indirect Effects of Low-Energy Electrons on DNA.* Annual Review of Physical Chemistry, 2015. **66**(1): p. 379-398.

29. Holley, A.K., et al., *Redox-modulated phenomena and radiation therapy: the central role of superoxide dismutases.* Antioxidants & redox signaling, 2014. **20**(10): p. 1567-1589.

30. Hubenko, K., et al., *Reactive oxygen species generation in aqueous solutions containing GdVO4:Eu3+ nanoparticles and their complexes with methylene blue.* Nanoscale Research Letters, 2018. **13**(1): p. 100.

31. Azzam, E.I., J.-P. Jay-Gerin, and D. Pain, *Ionizing radiation-induced metabolic oxidative stress and prolonged cell injury.* Cancer letters, 2012. **327**(1-2): p. 48-60.

32. Nikjoo, H., et al., *Computational Approach for Determining the Spectrum of DNA Damage Induced by Ionizing Radiation.* Radiation Research, 2001. **156**(5): p. 577-583.

33. *DNA Double Strand Break Repair: A Radiation Perspective.* Antioxidants & Redox Signaling, 2013. **18**(18): p. 2458-2472.

34. Sachs, R.K., et al., *DNA damage caused by ionizing radiation.* Mathematical Biosciences, 1992. **112**(2): p. 271-303.

35. Biau, J., et al., *Altering DNA Repair to Improve Radiation Therapy: Specific and Multiple Pathway Targeting.* Frontiers in Oncology, 2019. **9**(1009).

36. Mavragani, I.V., et al., *Ionizing Radiation and Complex DNA Damage: From Prediction to Detection Challenges and Biological Significance.* Cancers, 2019. **11**(11): p. 1789.

37. Kobayashi, K., et al., *Enhancement of radiation effect by heavy elements.* Mutation Research/Reviews in Mutation Research, 2010. **704**(1): p. 123-131.

38. Porcel, E., et al., *Gadolinium-based nanoparticles to improve the hadrontherapy performances.* Nanomedicine: Nanotechnology, Biology and Medicine, 2014. **10**(8): p. 1601-1608.

39. Hainfeld, J.F., et al., *Radiotherapy enhancement with gold nanoparticles.* Journal of Pharmacy and Pharmacology, 2008. **60**(8): p. 977-985.

40. Baker, S., et al., *A critical review of recent developments in radiotherapy for non-small cell lung cancer.* Radiation Oncology, 2016. **11**(1): p. 115.

41. Giaj-Levra, N., F. Ricchetti, and F. Alongi, *What is changing in radiotherapy for the treatment of locally advanced nonsmall cell lung cancer patients? A review.* Cancer Investigation, 2016. **34**(2): p. 80-93.

42. Bradley, J., et al., *Toxicity and outcome results of RTOG 9311: A phase I–II dose-escalation study using three-dimensional conformal radiotherapy in patients with inoperable non–small-cell lung carcinoma.* International Journal of Radiation Oncology, Biology, Physics, 2005. **61**(2): p. 318-328.

43. Milano, M.T., L.S. Constine, and P. Okunieff, *Normal Tissue Tolerance Dose Metrics for Radiation Therapy of Major Organs.* Seminars in Radiation Oncology, 2007. **17**(2): p. 131-140.

44. Jaffray, D.A., *Image-guided radiotherapy: from current concept to future perspectives.* Nat Rev Clin Oncol, 2012. **9**(12): p. 688-99.

45. Wang, H., et al., *Cancer Radiosensitizers.* Trends Pharmacol Sci, 2018. **39**(1): p. 24-48.

46. Lawrence, T.S., A.W. Blackstock, and C. McGinn, *The mechanism of action of radiosensitization of conventional chemotherapeutic agents.* Seminars in Radiation Oncology, 2003. **13**(1): p. 13-21.

47. Hashimoto, S., H. Anai, and K. Hanada, *Mechanisms of interstrand DNA crosslink repair and human disorders.* Genes and Environment, 2016. **38**(1): p. 9.

48. Rohde, D., et al., *Induction of drug-resistant bladder carcinoma cells in vitro: impact on polychemotherapy with cisplatin, methotrexate and vinblastine (CMV).* Urol Res, 1998. **26**(4): p. 249-57.

49. Verma, V., C.B. Simone, 2nd, and M. Werner-Wasik, *Acute and Late Toxicities of Concurrent Chemoradiotherapy for Locally-Advanced Non-Small Cell Lung Cancer.* Cancers, 2017. **9**(9): p. 120.

50. Curran, W.J., Jr., et al., *Sequential vs. concurrent chemoradiation for stage III non-small cell lung cancer: randomized phase III trial RTOG 9410.* J Natl Cancer Inst, 2011. **103**(19): p. 1452-60.

51. Boateng, F. and W. Ngwa, *Delivery of Nanoparticle-Based Radiosensitizers for Radiotherapy Applications.* International journal of molecular sciences, 2019. **21**(1): p. 273.

52. Lu, S.L., et al., *Enhanced Radiosensitization for Cancer Treatment with Gold Nanoparticles through Sonoporation.* Int J Mol Sci, 2020. **21**(21).

53. Azizi, S., et al., *Preparation of bismuth sulfide nanoparticles as targeted biocompatible nano-radiosensitizer and carrier of methotrexate.* Applied Organometallic Chemistry, 2020. **34**(1): p. e5251.

54. Chithrani, D.B., et al., *Gold Nanoparticles as Radiation Sensitizers in Cancer Therapy.* Radiation Research, 2010. **173**(6): p. 719-728.

55. Castillo, M.H., et al., *Effects of radiotherapy on mandibular reconstruction plates.* The American Journal of Surgery, 1988. **156**(4): p. 261-263.

56. Allal, A.S., et al., *Dose variation at bone/titanium interfaces using titanium hollow screw osseointegrating reconstruction plates.* Int J Radiat Oncol Biol Phys, 1998. **40**(1): p. 215-9.

57. Song, G., et al., *Emerging Nanotechnology and Advanced Materials for Cancer Radiation Therapy.* Advanced Materials, 2017. **29**(32): p. 1700996.

58. Butterworth, K.T., et al., *Physical basis and biological mechanisms of gold nanoparticle radiosensitization.* Nanoscale, 2012. **4**(16): p. 4830-8.

59. Rabus, H., et al., *Determining dose enhancement factors of high-Z nanoparticles from simulations where lateral secondary particle disequilibrium exists.* Physics in Medicine & Biology, 2019. **64**(15): p. 155016.

60. Evans, R.D., *Compton Effect,* in *Corpuscles and Radiation in Matter II / Korpuskeln und Strahlung in Materie II,* S. Flügge, Editor. 1958, Springer Berlin Heidelberg: Berlin, Heidelberg. p. 218-298.

61. Habiba, K., et al., *Enhancing Colorectal Cancer Radiation Therapy Efficacy using Silver Nanoprisms Decorated with Graphene as Radiosensitizers.* Scientific Reports, 2019. **9**(1): p. 17120.

62. Ku, A., et al., *Auger electrons for cancer therapy - a review.* EJNMMI radiopharmacy and chemistry, 2019. **4**(1): p. 27-27.

63. Jeynes, J.C., et al., *Investigation of gold nanoparticle radiosensitization mechanisms using a free radical scavenger and protons of different energies.* Phys Med Biol, 2014. **59**(21): p. 6431-43.

64. Retif, P., et al., *Nanoparticles for Radiation Therapy Enhancement: the Key Parameters.* Theranostics, 2015. **5**(9): p. 1030-1044.

65. Pan, X., et al., *Dissociative Electron Attachment to DNA.* Physical Review Letters, 2003. **90**(20): p. 208102.

66. Giglia-Mari, G., A. Zotter, and W. Vermeulen, *DNA damage response.* Cold Spring Harbor perspectives in biology, 2011. **3**(1): p. a000745-a000745.

67. Mah, L.J., A. El-Osta, and T.C. Karagiannis, *γH2AX: a sensitive molecular marker of DNA damage and repair.* Leukemia, 2010. **24**(4): p. 679-686.

68. Schultz, L.B., et al., *p53 binding protein 1 (53BP1) is an early participant in the cellular response to DNA double-strand breaks.* J Cell Biol, 2000. **151**(7): p. 1381-90.

69. Rogakou, E.P., et al., *DNA double-stranded breaks induce histone H2AX phosphorylation on serine 139.* J Biol Chem, 1998. **273**(10): p. 5858-68.

70. Rogakou, E.P., et al., *Megabase chromatin domains involved in DNA double-strand breaks in vivo.* J Cell Biol, 1999. **146**(5): p. 905-16.

71. Scarpato, R., et al., *Kinetics of nuclear phosphorylation (γ-H2AX) in human lymphocytes treated in vitro with UVB, bleomycin and mitomycin C.* Mutagenesis, 2013. **28**(4): p. 465-473.

72. Svetlova, M., et al., *Elimination of radiation-induced gamma-H2AX foci in mammalian nucleus can occur by histone exchange.* Biochem Biophys Res Commun, 2007. **358**(2): p. 650-4.

73. Mariotti, L.G., et al., *Use of the γ-H2AX assay to investigate DNA repair dynamics following multiple radiation exposures.* PloS one, 2013. **8**(11): p. e79541-e79541.

74. Boss, M.-K. and M. Dewhirst, *A Tribute to Philip Marcus and the Development of the Clonogenic Assay.* Radiation Research, 2015. **183**(5): p. 497-500, 4.

75. Munshi, A., M. Hobbs, and R.E. Meyn, *Clonogenic Cell Survival Assay*, in *Chemosensitivity: Volume 1 In Vitro Assays*, R.D. Blumenthal, Editor. 2005, Humana Press: Totowa, NJ. p. 21-28.

76. Subiel, A., R. Ashmore, and G. Schettino, *Standards and Methodologies for Characterizing Radiobiological Impact of High-Z Nanoparticles.* Theranostics, 2016. **6**(10): p. 1651-1671.

77. Matsui, T., et al., *Robustness of Clonogenic Assays as a Biomarker for Cancer Cell Radiosensitivity.* International journal of molecular sciences, 2019. **20**(17): p. 4148.

78. Dunne, A.L., et al., *Relationship between clonogenic radiosensitivity, radiation-induced apoptosis and DNA damage/repair in human colon cancer cells.* Br J Cancer, 2003. **89**(12): p. 2277-83.

79. Lin, S.H., et al., *A high content clonogenic survival drug screen identifies mek inhibitors as potent radiation sensitizers for KRAS mutant non-small-cell lung cancer.* J Thorac Oncol, 2014. **9**(7): p. 965-973.

80. Ma, M., et al., *Bi2S3-embedded mesoporous silica nanoparticles for efficient drug delivery and interstitial radiotherapy sensitization.* Biomaterials, 2015. **37**: p. 447-455.

81. Marill, J., et al., *Hafnium oxide nanoparticles: toward an in vitropredictive biological effect?* Radiation Oncology, 2014. **9**(1): p. 150.

82. Luchette, M., et al., *Radiation dose enhancement of gadolinium-based AGuIX nanoparticles on HeLa cells.* Nanomedicine: Nanotechnology, Biology and Medicine, 2014. **10**(8): p. 1751-1755.

83. Gong, T., et al., *Full-Process Radiosensitization Based on Nanoscale Metal–Organic Frameworks.* ACS Nano, 2020. **14**(3): p. 3032-3040.

84. Zhang, P., et al., *Radiotherapy-Activated Hafnium Oxide Nanoparticles Produce Abscopal Effect in a Mouse Colorectal Cancer Model.* Int J Nanomedicine, 2020. **15**: p. 3843-3850.

85. Shukla, R., et al., *Biocompatibility of Gold Nanoparticles and Their Endocytotic Fate Inside the Cellular Compartment: A Microscopic Overview.* Langmuir, 2005. **21**(23): p. 10644-10654.

86. Haume, K., et al., *Gold nanoparticles for cancer radiotherapy: a review.* Cancer Nanotechnol, 2016. **7**(1): p. 8.

87. Zhang, X.D., et al., *Size-dependent radiosensitization of PEG-coated gold nanoparticles for cancer radiation therapy.* Biomaterials, 2012. **33**(27): p. 6408-19.

88. Longmire, M., P.L. Choyke, and H. Kobayashi, *Clearance properties of nano-sized particles and molecules as imaging agents: considerations and caveats.* Nanomedicine (Lond), 2008. **3**(5): p. 703-17.

89. Bertrand, N. and J.C. Leroux, *The journey of a drug-carrier in the body: an anatomo-physiological perspective.* J Control Release, 2012. **161**(2): p. 152-63.

90. Tsoli, M., et al., *Cellular uptake and toxicity of Au55 clusters.* Small, 2005. **1**(8-9): p. 841-4.

91. Liu, Z., et al., *Enhancement of radiotherapy efficacy by silver nanoparticles in hypoxic glioma cells.* Artif Cells Nanomed Biotechnol, 2018. **46**(sup3): p. S922-s930.

92. Zhao, J., et al., *Enhancement of Radiosensitization by Silver Nanoparticles Functionalized with Polyethylene Glycol and Aptamer As1411 for Glioma Irradiation Therapy.* International journal of nanomedicine, 2019. **14**: p. 9483-9496.

93. Abdellatif, A.A.H., et al., *Silver Citrate Nanoparticles Inhibit PMA-Induced TNFα Expression via Deactivation of NF-κB Activity in Human Cancer Cell-Lines, MCF-7.* Int J Nanomedicine, 2020. **15**: p. 8479-8493.

94. Ema, M., et al., *A review of reproductive and developmental toxicity of silver nanoparticles in laboratory animals.* Reprod Toxicol, 2017. **67**: p. 149-164.

95. Hadrup, N., et al., *The similar neurotoxic effects of nanoparticulate and ionic silver in vivo and in vitro.* Neurotoxicology, 2012. **33**(3): p. 416-23.

96. Ong, C., et al., *Silver nanoparticles disrupt germline stem cell maintenance in the Drosophila testis.* Sci Rep, 2016. **6**: p. 20632.

97. Fathi, N., et al., *The effect of silver nanoparticles on the reproductive system of adult male rats: A morphological, histological and DNA integrity study.* Adv Clin Exp Med, 2019. **28**(3): p. 299-305.

98. Andoh, T., et al., *Influence of the particle size of gadolinium-loaded chitosan nanoparticles on their tumor-killing effect in neutron capture therapy in vitro.* Appl Radiat Isot, 2020. **164**: p. 109270.

99. Liu, W., et al., *Tumor-targeted pH-low insertion peptide delivery of theranostic gadolinium nanoparticles for image-guided nanoparticle-enhanced radiation therapy.* Translational oncology, 2020. **13**(11): p. 100839-100839.

100. Verry, C., et al., *MRI-guided clinical 6-MV radiosensitization of glioma using a unique gadolinium-based nanoparticles injection.* Nanomedicine, 2016. **11**(18): p. 2405-2417.

101. Shen, C., et al., *Phase I study of NBTXR3 activated by radiotherapy in patients with advanced cancers treated with an anti-PD-1 therapy.* Journal of Clinical Oncology, 2020. **38**(15_suppl): p. TPS3173-TPS3173.

102. Bonvalot, S., et al., *NBTXR3, a first-in-class radioenhancer hafnium oxide nanoparticle, plus radiotherapy versus radiotherapy alone in patients with locally advanced soft-tissue sarcoma (Act.In.Sarc): a multicentre, phase 2–3, randomised, controlled trial.* The Lancet Oncology, 2019. **20**(8): p. 1148-1159.

103. Detappe, A., et al., *Correction to "Ultrasmall Silica-Based Bismuth Gadolinium Nanoparticles for Dual Magnetic Resonance-Computed Tomography Image Guided Radiation Therapy".* Nano Lett, 2020. **20**(8): p. 6223.

CHAPTER 2:

1. Sagbas, S. and N. Sahiner, *22 - Carbon dots: preparation, properties, and application*, in *Nanocarbon and its Composites*, A. Khan, et al., Editors. 2019, Woodhead Publishing. p. 651-676.
2. Wang, Y., et al., *Fluorescent carbon dots: rational synthesis, tunable optical properties and analytical applications.* RSC Advances, 2017. **7**(65): p. 40973-40989.
3. Yang, Y., et al., *iRGD-decorated red shift emissive carbon nanodots for tumor targeting fluorescence imaging.* J Colloid Interface Sci, 2018. **509**: p. 515-521.
4. Sun, S., et al., *Highly luminescence manganese doped carbon dots.* Chinese Chemical Letters, 2019. **30**(5): p. 1051-1054.
5. Sri, S., et al., *Highly Biocompatible, Fluorescence, and Zwitterionic Carbon Dots as a Novel Approach for Bioimaging Applications in Cancerous Cells.* ACS Appl Mater Interfaces, 2018. **10**(44): p. 37835-37845.
6. Wang, J., S. Su, and J. Qiu, *Biocompatible Carbon Dots with Diverse Surface Modification.* MRS Advances, 2016. **1**(19): p. 1333-1338.
7. Zhang, R., et al., *Preparation of high-quality biocompatible carbon dots by extraction, with new thoughts on the luminescence mechanisms.* Nanotechnology, 2013. **24**(22): p. 225601.
8. Moonrinta, S., et al., *Synthesis of biocompatible carbon dots from yogurt and gas vapor sensing.* IOP Conference Series: Materials Science and Engineering, 2018. **378**: p. 012005.

9. Erickson, H.P., *Size and shape of protein molecules at the nanometer level determined by sedimentation, gel filtration, and electron microscopy.* Biological procedures online, 2009. **11**: p. 32-51.

10. Liu, J., et al., *Renal clearable inorganic nanoparticles: a new frontier of bionanotechnology.* Materials Today, 2013. **16**(12): p. 477-486.

11. Longmire, M., P.L. Choyke, and H. Kobayashi, *Clearance properties of nano-sized particles and molecules as imaging agents: considerations and caveats.* Nanomedicine (London, England), 2008. **3**(5): p. 703-717.

12. Hettiarachchi, S.D., et al., *Triple conjugated carbon dots as a nano-drug delivery model for glioblastoma brain tumors.* Nanoscale, 2019. **11**(13): p. 6192-6205.

13. Qian, M., et al., *Highly Crystalline Multicolor Carbon Nanodots for Dual-Modal Imaging-Guided Photothermal Therapy of Glioma.* ACS Applied Materials & Interfaces, 2018. **10**(4): p. 4031-4040.

14. Wei, X., et al., *Green Synthesis of Fluorescent Carbon Dots from Gynostemma for Bioimaging and Antioxidant in Zebrafish.* ACS Applied Materials & Interfaces, 2019. **11**(10): p. 9832-9840.

15. Wang, M., et al., *Green synthesis of carbon dots using the flowers of Osmanthus fragrans (Thunb.) Lour. as precursors: application in Fe3+ and ascorbic acid determination and cell imaging.* Analytical and Bioanalytical Chemistry, 2019. **411**(12): p. 2715-2727.

16. Lai, Z., et al., *Green Synthesis of Fluorescent Carbon Dots from Cherry Tomatoes for Highly Effective Detection of Trifluralin Herbicide in Soil Samples.* ChemistrySelect, 2020. **5**(6): p. 1956-1960.

17. Chen, H., et al., *Gd-Encapsulated Carbonaceous Dots with Efficient Renal Clearance for Magnetic Resonance Imaging.* Advanced Materials, 2014. **26**(39): p. 6761-6766.

18. Schipper, M.L., et al., *A pilot toxicology study of single-walled carbon nanotubes in a small sample of mice.* Nature Nanotechnology, 2008. **3**(4): p. 216-221.

19. Ersoy, H. and F.J. Rybicki, *Biochemical safety profiles of gadolinium-based extracellular contrast agents and nephrogenic systemic fibrosis.* J Magn Reson Imaging, 2007. **26**(5): p. 1190-7.

20. Yang, J.-S., B.-Z. Yu, and W.-X. Li, *A new potential radiosensitizer: ammonium persulfate modified WCNTs.* Nature Precedings, 2008.

21. Ni, J., et al., *Cytotoxic and radiosensitizing effects of nano-C60 on tumor cells in vitro.* Journal of Nanoparticle Research, 2008. **10**(4): p. 643-651.

22. Kato, S., M. Kimura, and N. Miwa, *Radiosensitization by fullerene-C60 dissolved in squalene on human malignant melanoma through lipid peroxidation and enhanced mitochondrial membrane potential.* Radiation Physics and Chemistry, 2014. **97**: p. 134-141.

23. Xia, C., et al., *Evolution and Synthesis of Carbon Dots: From Carbon Dots to Carbonized Polymer Dots.* Advanced Science, 2019. **6**(23): p. 1901316.

24. Sharma, A. and J. Das, *Small molecules derived carbon dots: synthesis and applications in sensing, catalysis, imaging, and biomedicine.* Journal of Nanobiotechnology, 2019. **17**(1): p. 92.

25. Thongpool, V., P. Asanithi, and P. Limsuwan, *Synthesis of Carbon Particles using Laser Ablation in Ethanol.* Procedia Engineering, 2012. **32**: p. 1054-1060.

26. Reyes, D., et al., *Laser Ablated Carbon Nanodots for Light Emission.* Nanoscale Research Letters, 2016. **11**(1): p. 424.

27. Liu, M., et al., *Carbon quantum dots directly generated from electrochemical oxidation of graphite electrodes in alkaline alcohols and the applications for specific ferric ion detection and cell imaging.* Analyst, 2016. **141**(9): p. 2657-2664.

28. Ahirwar, S., S. Mallick, and D. Bahadur, *Electrochemical Method To Prepare Graphene Quantum Dots and Graphene Oxide Quantum Dots.* ACS Omega, 2017. **2**(11): p. 8343-8353.

29. Russo, C., B. Apicella, and A. Ciajolo, *Blue and green luminescent carbon nanodots from controllable fuel-rich flame reactors.* Scientific Reports, 2019. **9**(1): p. 14566.

30. Yang, H., et al., *Fluorescent carbon dots synthesized by microwave-assisted pyrolysis for chromium(VI) and ascorbic acid sensing and logic gate operation.* Spectrochimica Acta Part A: Molecular and Biomolecular Spectroscopy, 2018. **205**: p. 12-20.

31. Qiao, Z.-A., et al., *Commercially activated carbon as the source for producing multicolor photoluminescent carbon dots by chemical oxidation.* Chemical Communications, 2010. **46**(46): p. 8812-8814.

32. Xia, C., et al., *Evolution and Synthesis of Carbon Dots: From Carbon Dots to Carbonized Polymer Dots.* Advanced science (Weinheim, Baden-Wurttemberg, Germany), 2019. **6**(23): p. 1901316-1901316.

33. Xie, Y., et al., *Green Hydrothermal Synthesis of N-doped Carbon Dots from Biomass Highland Barley for the Detection of Hg(2).* Sensors (Basel, Switzerland), 2019. **19**(14): p. 3169.

34. Yang, Y., et al., *Bottom-up fabrication of photoluminescent carbon dots with uniform morphology via a soft–hard template approach.* Chemical Communications, 2013. **49**(43): p. 4920-4922.

35. Kim, H.H., et al., *Bottom-Up Synthesis of Carbon Quantum Dots With High Performance Photo- and Electroluminescence.* Particle & Particle Systems Characterization, 2018. **35**(7): p. 1800080.

36. Song, Y., et al., *Drug-Derived Bright and Color-Tunable N-Doped Carbon Dots for Cell Imaging and Sensitive Detection of Fe3+ in Living Cells.* ACS Applied Materials & Interfaces, 2017. **9**(8): p. 7399-7405.

37. Chen, H., et al., *Mesoporous Silica as Nanoreactors to Prepare Gd-Encapsulated Carbon Dots of Controllable Sizes and Magnetic Properties.* Advanced Functional Materials, 2016. **26**(22): p. 3973-3982.

CHAPTER 3:

1. Song, G.;Cheng, L.;Chao, Y.;Yang, K.; Liu, Z. Emerging Nanotechnology and Advanced Materials for Cancer Radiation Therapy. *Adv. Mater.* **2017**, *29*, 1700996.

2. Hao, Y.;Altundal, Y.;Moreau, M.;Sajo, E.;Kumar, R.; Ngwa, W. Potential for enhancing external beam radiotherapy for lung cancer using high-Z nanoparticles administered via inhalation. *Phys. Med. Biol.* **2015**, *60*, 7035-7043.

3. Kim, D.; Wang, I. MO-F-213AB-06: Experimental Evaluation of Radiation Dose Effect by High Atomic Number Materials for Superficial Radiation Therapy. *Med. Phys.* **2012**, *39*, 3872.
4. Bonvalot, S.;Le Pechoux, C.;De Baere, T.;Kantor, G.;Buy, X.;Stoeckle, E.;Terrier, P.;Sargos, P.;Coindre, J. M.;Lassau, N.;Ait Sarkouh, R.;Dimitriu, M.;Borghi, E.;Levy, L.;Deutsch, E.; Soria, J. C. First-in-Human Study Testing a New Radioenhancer Using Nanoparticles (NBTXR3) Activated by Radiation Therapy in Patients with Locally Advanced Soft Tissue Sarcomas. *Clin. Cancer Res.* **2017**, *23*, 908-917.
5. Deng, J.;Xu, S.;Hu, W.;Xun, X.;Zheng, L.; Su, M. Tumor targeted, stealthy and degradable bismuth nanoparticles for enhanced X-ray radiation therapy of breast cancer. *Biomaterials* **2018**, *154*, 24-33.
6. Detappe, A.;Thomas, E.;Tibbitt, M. W.;Kunjachan, S.;Zavidij, O.;Parnandi, N.;Reznichenko, E.;Lux, F.;Tillement, O.; Berbeco, R. Ultrasmall Silica-Based Bismuth Gadolinium Nanoparticles for Dual Magnetic Resonance–Computed Tomography Image Guided Radiation Therapy. *Nano Lett.* **2017**, *17*, 1733-1740.
7. Hainfeld, J. F.;Dilmanian, F. A.;Zhong, Z.;Slatkin, D. N.;Kalef-Ezra, J. A.; Smilowitz, H. M. Gold nanoparticles enhance the radiation therapy of a murine squamous cell carcinoma. *Phys. Med. Biol.* **2010**, *55*, 3045-3059.
8. Li, Y.;Yun, K. H.;Lee, H.;Goh, S. H.;Suh, Y. G.; Choi, Y. Porous platinum nanoparticles as a high-Z and oxygen generating nanozyme for enhanced radiotherapy in vivo. *Biomaterials* **2019**, *197*, 12-19.

9. Zhang, M.;Cui, Z.;Song, R.;Lv, B.;Tang, Z.;Meng, X.;Chen, X.;Zheng, X.;Zhang, J.;Yao, Z.; Bu, W. SnWO4-based nanohybrids with full energy transfer for largely enhanced photodynamic therapy and radiotherapy. *Biomaterials* **2018**, *155*, 135-144.

10. Changizi, O.;Khoei, S.;Mahdavian, A.;Shirvalilou, S.;Mahdavi, S. R.; Rad, J. K. Enhanced radiosensitivity of LNCaP prostate cancer cell line by gold-photoactive nanoparticles modified with folic acid. *Photodiagn. Photodyn. Ther.* **2020**, *29*, 101602.

11. Saberi, A.;Shahbazi-Gahrouei, D.;Abbasian, M.;Fesharaki, M.;Baharlouei, A.; Arab-Bafrani, Z. Gold nanoparticles in combination with megavoltage radiation energy increased radiosensitization and apoptosis in colon cancer HT-29 cells. *Int. J. Radiat. Biol.* **2017**, *93*, 315-323.

12. Bonvalot, S.;Rutkowski, P. L.;Thariat, J.;Carrere, S.;Ducassou, A.;Sunyach, M. P.;Agoston, P.;Hong, A.;Mervoyer, A.;Rastrelli, M.;Moreno, V.;Li, R. K.;Tiangco, B.;Herraez, A. C.;Gronchi, A.;Mangel, L.;Sy-Ortin, T.;Hohenberger, P.;de Baere, T.;Le Cesne, A.;Helfre, S.;Saada-Bouzid, E.;Borkowska, A.;Anghel, R.;Co, A.;Gebhart, M.;Kantor, G.;Montero, A.;Loong, H. H.;Verges, R.;Lapeire, L.;Dema, S.;Kacso, G.;Austen, L.;Moureau-Zabotto, L.;Servois, V.;Wardelmann, E.;Terrier, P.;Lazar, A. J.;Bovee, J.;Le Pechoux, C.; Papai, Z. NBTXR3, a first-in-class radioenhancer hafnium oxide nanoparticle, plus radiotherapy versus radiotherapy alone in patients with locally advanced soft-tissue sarcoma (Act.In.Sarc): a multicentre, phase 2-3, randomised, controlled trial. *Lancet Oncol.* **2019**, *20*, 1148-1159.

13. Rajaee, A.;Wang, S.;Zhao, L.;Wang, D.;Liu, Y.;Wang, J.; Ying, K. Multifunction bismuth gadolinium oxide nanoparticles as radiosensitizer in radiation therapy and imaging. *Phys. Med. Biol.* **2019**, *64*, 195007.

14. Wu, B.;Lu, S. T.;Yu, H.;Liao, R. F.;Li, H.;Lucie Zafitatsimo, B. V.;Li, Y. S.;Zhang, Y.;Zhu, X. L.;Liu, H. G.;Xu, H. B.;Huang, S. W.; Cheng, Z. Gadolinium-chelate functionalized bismuth nanotheranostic agent for in vivo MRI/CT/PAI imaging-guided photothermal cancer therapy. *Biomaterials* **2018**, *159*, 37-47.

15. Yong, Y.;Cheng, X.;Bao, T.;Zu, M.;Yan, L.;Yin, W.;Ge, C.;Wang, D.;Gu, Z.; Zhao, Y. Tungsten Sulfide Quantum Dots as Multifunctional Nanotheranostics for In Vivo Dual-Modal Image-Guided Photothermal/Radiotherapy Synergistic Therapy. *ACS Nano* **2015**, *9*, 12451-12463.

16. Zang, Y.;Gong, L.;Mei, L.;Gu, Z.; Wang, Q. Bi2WO6 Semiconductor Nanoplates for Tumor Radiosensitization through High- Z Effects and Radiocatalysis. *ACS Appl. Mater. Interfaces* **2019**, *11*, 18942-18952.

17. Kolosnjaj-Tabi, J.;Javed, Y.;Lartigue, L.;Volatron, J.;Elgrabli, D.;Marangon, I.;Pugliese, G.;Caron, B.;Figuerola, A.;Luciani, N.;Pellegrino, T.;Alloyeau, D.; Gazeau, F. The One Year Fate of Iron Oxide Coated Gold Nanoparticles in Mice. *ACS Nano* **2015**, *9*, 7925-7939.

18. Chen, H.;Qiu, Y.;Ding, D.;Lin, H.;Sun, W.;Wang, G. D.;Huang, W.;Zhang, W.;Lee, D.;Liu, G.;Xie, J.; Chen, X. Gadolinium-Encapsulated Graphene Carbon Nanotheranostics for Imaging-Guided Photodynamic Therapy. *Adv. Mater.* **2018**, *30*, 1802748.

19. Chen, H.;Wang, G. D.;Tang, W.;Todd, T.;Zhen, Z.;Tsang, C.;Hekmatyar, K.;Cowger, T.;Hubbard, R.;Zhang, W.;Stickney, J.;Shen, B.; Xie, J. Gd-encapsulated carbonaceous dots with efficient renal clearance for magnetic resonance imaging. *Adv. Mater.* **2014**, *26*, 6761-6766.

20. He, X.;Luo, Q.;Zhang, J.;Chen, P.;Wang, H. J.;Luo, K.; Yu, X. Q. Gadolinium-doped carbon dots as nano-theranostic agents for MR/FL diagnosis and gene delivery. *Nanoscale* **2019**, *11*, 12973-12982.

21. Xu, Y.;Jia, X. H.;Yin, X. B.;He, X. W.; Zhang, Y. K. Carbon quantum dot stabilized gadolinium nanoprobe prepared via a one-pot hydrothermal approach for magnetic resonance and fluorescence dual-modality bioimaging. *Anal. Chem.* **2014**, *86*, 12122-12129.

22. Schipper, M. L.;Nakayama-Ratchford, N.;Davis, C. R.;Kam, N. W.;Chu, P.;Liu, Z.;Sun, X.;Dai, H.; Gambhir, S. S. A pilot toxicology study of single-walled carbon nanotubes in a small sample of mice. *Nat. Nanotechnol.* **2008**, *3*, 216-221.

23. Jemal, A.;Siegel, R.;Xu, J.; Ward, E. Cancer statistics, 2010. *CA Cancer J. Clin.* **2010**, *60*, 277-300.

24. Baker, S.;Dahele, M.;Lagerwaard, F. J.; Senan, S. A critical review of recent developments in radiotherapy for non-small cell lung cancer. *Radiat. Oncol.* **2016**, *11*, 115.

25. Bradley, J. D.;Paulus, R.;Komaki, R.;Masters, G.;Blumenschein, G.;Schild, S.;Bogart, J.;Hu, C.;Forster, K.;Magliocco, A.;Kavadi, V.;Garces, Y. I.;Narayan, S.;Iyengar, P.;Robinson, C.;Wynn, R. B.;Koprowski, C.;Meng, J.;Beitler, J.;Gaur, R.;Curran, W., Jr.; Choy, H. Standard-dose versus high-dose conformal

radiotherapy with concurrent and consolidation carboplatin plus paclitaxel with or without cetuximab for patients with stage IIIA or IIIB non-small-cell lung cancer (RTOG 0617): a randomised, two-by-two factorial phase 3 study. *Lancet Oncol.* **2015**, *16*, 187-199.

26. Luffer, D. R.; Schram, K. H. Electron ionization mass spectrometry of synthetic C60. *Rapid Communications in Mass Spectrometry* **1990**, *4*, 552-556.

27. O'Brien, S. C.;Heath, J. R.;Curl, R. F.; Smalley, R. E. Photophysics of buckminsterfullerene and other carbon cluster ions. *J. Chem. Phys.* **1988**, *88*, 220-230.

28. Chen, H.;Wang, G. D.;Sun, X.;Todd, T.;Zhang, F.;Xie, J.; Shen, B. Mesoporous Silica as Nanoreactors to Prepare Gd-Encapsulated Carbon Dots of Controllable Sizes and Magnetic Properties. *Adv. Funct. Mater.* **2016**, *26*, 3973-3982.

29. Javaid, R.; Qazi, U. Y. Catalytic Oxidation Process for the Degradation of Synthetic Dyes: An Overview. *Int. J. Environ. Res. Public Health* **2019**, *16*, 2066.

30. Ncube, P.;Bingwa, N.;Baloyi, H.; Meijboom, R. Catalytic activity of palladium and gold dendrimer-encapsulated nanoparticles for methylene blue reduction: A kinetic analysis. *Appl. Catal., A* **2015**, *495*, 63-71.

31. Sun, L.;Hu, D.;Zhang, Z.; Deng, X. Oxidative Degradation of Methylene Blue via PDS-Based Advanced Oxidation Process Using Natural Pyrite. *Int. J. Environ. Res. Public Health* **2019**, *16*, 4773.

32. Li, S.;Timoshkin, I. V.;Maclean, M.;Macgregor, S. J.;Wilson, M. P.;Given, M. J.;Wang, T.; Anderson, J. G. Fluorescence detection of hydroxyl radicals in water

produced by atmospheric pulsed discharges. *IEEE Trans. Dielectr. Electr. Insul.* **2015**, *22*, 1856-1865.

33. Mason, T. J.;Lorimer, J. P.;Bates, D. M.; Zhao, Y. Dosimetry in sonochemistry: the use of aqueous terephthalate ion as a fluorescence monitor. *Ultrason. Sonochem.* **1994**, *1*, S91-S95.

34. Page, S. E.;Arnold, W. A.; McNeill, K. Terephthalate as a probe for photochemically generated hydroxyl radical. *J. Environ. Monit.* **2010**, *12*, 1658-1665.

35. Ragàs, X.;Jiménez-Banzo, A.;Sánchez-García, D.;Batllori, X.; Nonell, S. Singlet oxygen photosensitisation by the fluorescent probe Singlet Oxygen Sensor Green®. *Chem. Commun.* **2009**, *20*, 2920-2922.

36. Cheng, G.;Zielonka, J.;McAllister, D.;Hardy, M.;Ouari, O.;Joseph, J.;Dwinell, M. B.; Kalyanaraman, B. Antiproliferative effects of mitochondria-targeted cationic antioxidants and analogs: Role of mitochondrial bioenergetics and energy-sensing mechanism. *Cancer Lett.* **2015**, *365*, 96-106.

37. Marrache, S.; Dhar, S. Engineering of blended nanoparticle platform for delivery of mitochondria-acting therapeutics. *Proc. Natl. Acad. Sci. U.S.A.* **2012**, *109*, 16288-16293.

38. Retif, P.;Pinel, S.;Toussaint, M.;Frochot, C.;Chouikrat, R.;Bastogne, T.; Barberi-Heyob, M. Nanoparticles for Radiation Therapy Enhancement: the Key Parameters. *Theranostics* **2015**, *5*, 1030-1044.

39. Chithrani, D. B.;Jelveh, S.;Jalali, F.;van Prooijen, M.;Allen, C.;Bristow, R. G.;Hill, R. P.; Jaffray, D. A. Gold nanoparticles as radiation sensitizers in cancer therapy. *Radiat. Res.* **2010**, *173*, 719-728.

40. Rahman, W. N.;Bishara, N.;Ackerly, T.;He, C. F.;Jackson, P.;Wong, C.;Davidson, R.; Geso, M. Enhancement of radiation effects by gold nanoparticles for superficial radiation therapy. *Nanomed. Nanotechnol. Biol. Med.* **2009**, *5*, 136-142.

41. Liu, C.-J.;Wang, C.-H.;Chen, S.-T.;Chen, H.-H.;Leng, W.-H.;Chien, C.-C.;Wang, C.-L.;Kempson, I. M.;Hwu, Y.; Lai, T.-C. Enhancement of cell radiation sensitivity by pegylated gold nanoparticles. *Phys. Med. Biol.* **2010**, *55*, 931.

CHAPTER 4:

1. Rosenberg, A., et al., *Real-Time Fluorescence Imaging Using Indocyanine Green to Assess Therapeutic Effects of Near-Infrared Photoimmunotherapy in Tumor Model Mice.* Molecular Imaging, 2020. **19**.
2. Li, Z., S. Yao, and J. Xu, *Indocyanine-green-assisted near-infrared dental imaging - the feasibility of in vivo imaging and the optimization of imaging conditions.* Scientific Reports, 2019. **9**(1): p. 8238.
3. Li, Y., X. Xia, and Y.M. Paulus, *Advances in Retinal Optical Imaging.* Photonics, 2018. **5**(2): p. 9.
4. Men, X., et al., *Thermosensitive Polymer Dot Nanocomposites for Trimodal Computed Tomography/Photoacoustic/Fluorescence Imaging-Guided Synergistic Chemo-Photothermal Therapy.* ACS Applied Materials & Interfaces, 2020.
5. Nguyen, H.N.Y. and W. Steenbergen, *Feasibility of identifying reflection artifacts in photoacoustic imaging using two-wavelength excitation.* Biomedical Optics Express, 2020. **11**(10): p. 5745-5759.
6. Chinnathambi, S. and N. Shirahata, *Recent advances on fluorescent biomarkers of near-infrared quantum dots for in vitro and in vivo imaging.* Science and technology of advanced materials, 2019. **20**(1): p. 337-355.
7. Wang, L., et al., *Hybrid Rhodamine Fluorophores in the Visible/NIR Region for Biological Imaging.* Angewandte Chemie International Edition, 2019. **58**(40): p. 14026-14043.

8. Chang, X.-H., et al., *Research Progress of Near-Infrared Fluorescence Immunoassay*. Micromachines, 2019. **10**(6): p. 422.

9. Resch-Genger, U., et al., *Quantum dots versus organic dyes as fluorescent labels*. Nature Methods, 2008. **5**(9): p. 763-775.

10. Sun, Y., et al., *Beyond OLED: Efficient Quantum Dot Light-Emitting Diodes for Display and Lighting Application.* The Chemical Record, 2019. **19**(8): p. 1729-1752.

11. Xu, N., et al., *Imaging of water soluble CdTe/CdS core-shell quantum dots in inhibiting multidrug resistance of cancer cells.* Talanta, 2019. **201**: p. 309-316.

12. Winnik, F.M. and D. Maysinger, *Quantum Dot Cytotoxicity and Ways To Reduce It.* Accounts of Chemical Research, 2013. **46**(3): p. 672-680.

13. Zhao, L., et al., *New insights into the release mechanism of Cd(2+) from CdTe quantum dots within single cells in situ.* Ecotoxicol Environ Saf, 2020. **196**: p. 110569.

14. Ryman-Rasmussen, J.P., J.E. Riviere, and N.A. Monteiro-Riviere, *Surface Coatings Determine Cytotoxicity and Irritation Potential of Quantum Dot Nanoparticles in Epidermal Keratinocytes.* Journal of Investigative Dermatology, 2007. **127**(1): p. 143-153.

15. Ding, C., A. Zhu, and Y. Tian, *Functional Surface Engineering of C-Dots for Fluorescent Biosensing and in Vivo Bioimaging.* Accounts of Chemical Research, 2014. **47**(1): p. 20-30.

16. Du, F., et al., *Engineered gadolinium-doped carbon dots for magnetic resonance imaging-guided radiotherapy of tumors.* Biomaterials, 2017. **121**: p. 109-120.

17. Wang, Y. and A. Hu, *Carbon quantum dots: synthesis, properties and applications.* Journal of Materials Chemistry C, 2014. **2**(34): p. 6921-6939.

18. Yang, R., et al., *A fluorescent "on-off-on" assay for selective recognition of Cu(II) and glutathione based on modified carbon nanodots, and its application to cellular imaging.* Microchimica Acta, 2017. **184**(4): p. 1143-1150.

19. Guo, Y., et al., *Hydrothermal synthesis of highly fluorescent carbon nanoparticles from sodium citrate and their use for the detection of mercury ions.* Carbon, 2013. **52**: p. 583-589.

20. Liu, H., et al., *Graphitic Carbon Nitride Quantum Dots Embedded in Carbon Nanosheets for Near-Infrared Imaging-Guided Combined Photo-Chemotherapy.* ACS Nano, 2020. **14**(10): p. 13304-13315.

21. Yang, S.-T., et al., *Carbon Dots for Optical Imaging in Vivo.* Journal of the American Chemical Society, 2009. **131**(32): p. 11308-11309.

22. Zhu, S., et al., *Highly Photoluminescent Carbon Dots for Multicolor Patterning, Sensors, and Bioimaging.* Angewandte Chemie International Edition, 2013. **52**(14): p. 3953-3957.

23. Zheng, X.T., et al., *Glowing Graphene Quantum Dots and Carbon Dots: Properties, Syntheses, and Biological Applications.* Small, 2015. **11**(14): p. 1620-1636.

24. Lu, S., et al., *Near-Infrared Photoluminescent Polymer–Carbon Nanodots with Two-Photon Fluorescence.* Advanced Materials, 2017. **29**(15): p. 1603443.

25. Chen, H., et al., *Mesoporous Silica as Nanoreactors to Prepare Gd-Encapsulated Carbon Dots of Controllable Sizes and Magnetic Properties.* Advanced Functional Materials, 2016. **26**(22): p. 3973-3982.

26. Chen, H., et al., *Gd-Encapsulated Carbonaceous Dots with Efficient Renal Clearance for Magnetic Resonance Imaging.* Advanced Materials, 2014. **26**(39): p. 6761-6766.

27. Zhang, J. and S.-H. Yu, *Carbon dots: large-scale synthesis, sensing and bioimaging.* Materials Today, 2016. **19**(7): p. 382-393.

28. Kalavagunta, C., S. Michaeli, and G.J. Metzger, *In vitro Gd-DTPA relaxometry studies in oxygenated venous human blood and aqueous solution at 3 and 7 T.* Contrast Media & Molecular Imaging, 2014. **9**(2): p. 169-176.

APPENDICES

A Supporting information for Chapter 3

Abbreviation list

ALT	Alanine Aminotransferase
ATP	Adenosine Triphosphate
BUN	Urea Nitrogen
DLS	Dynamic Light Scattering
DMEM	Dulbecco's Modified Eagle's Medium
EDS	Energy Dispersive Spectroscopy
ESI	Electrospray Ionization
FBS	*Fetal Bovine Serum*
ICP-MS	Inductively Coupled Plasma Mass Spectrometry
LDI	Laser Desorption Ionization
MRI	Magnetic Resonance Imaging
MTT	3-(4,5-Dimethylthiazolyl-2)-2,5-diphenyltetrazolium bromide
NPs	Nanoparticles
PBS	*Phosphate-Buffered Saline*
REF	*Radiation Enhancement Factor*
ROS	*Reactive Oxygen Species*
RPMI 1640	Roswell Park Memorial Institute Medium 1640
RT	Radiation
SEM	Scanning Electron Microscopy
SOD	Superoxide Dismutase
SOSG	Singlet Oxygen Sensor Green
STEM	Scanning Transmission Electron Microscopy
TA	Terephthalic Acid

TEM	Transmission Electron Microscopy

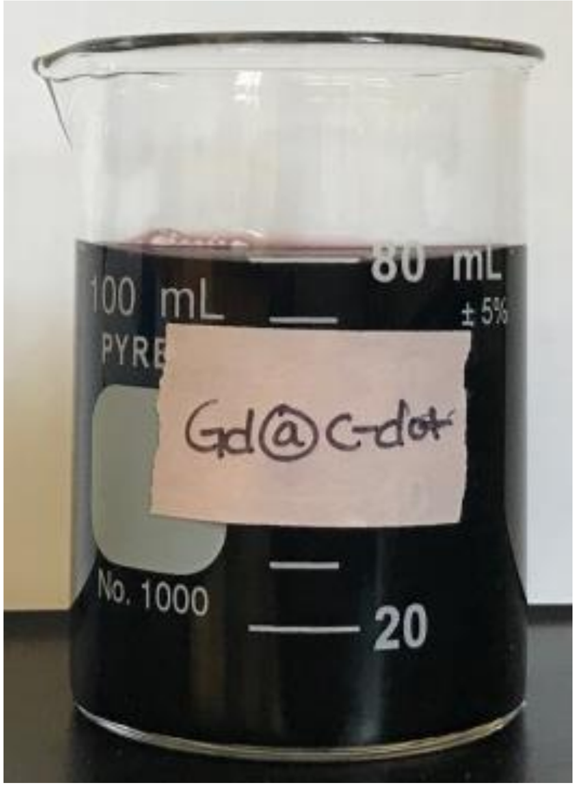

Figure S1. As-synthesized of Gd@Cdots dispersed in water.

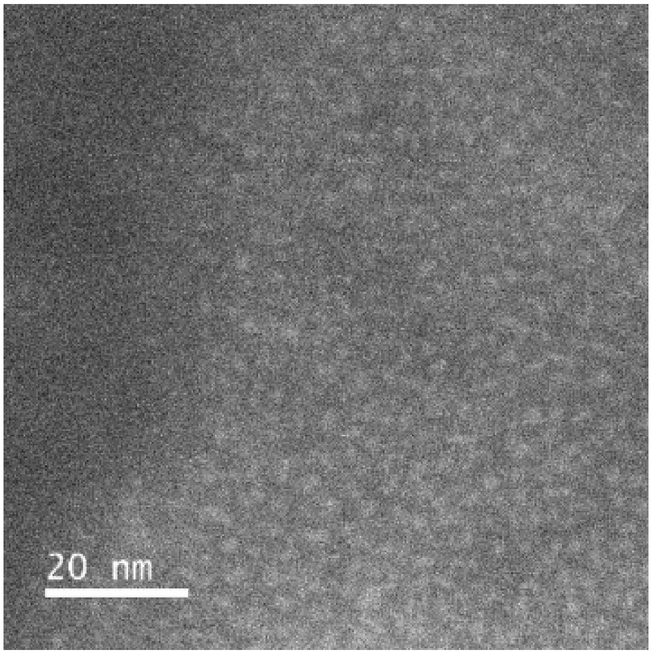

Figure S2. STEM image of Gd@Cdots.

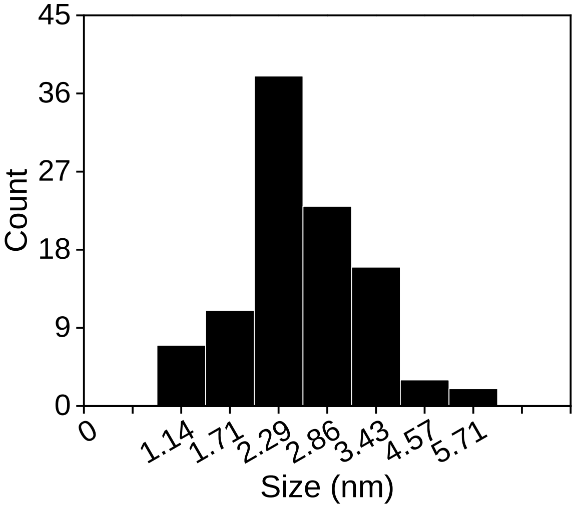

Figure S3. Statics on size distribution of Gd@Cdots, based on the TEM results.

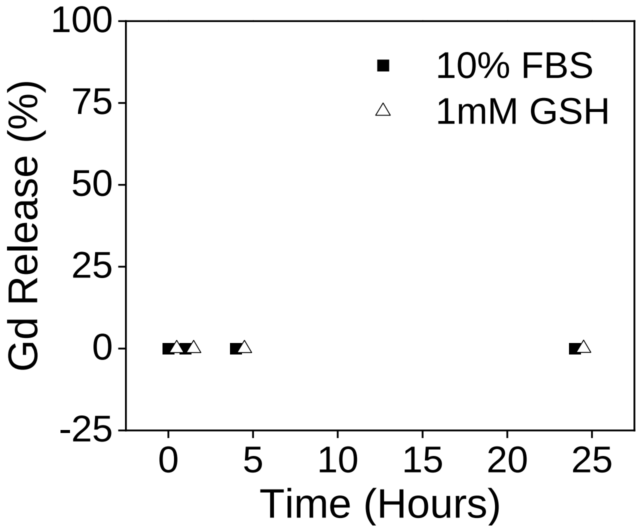

Figure S4. Gd release when Gd@Cdots were incubated in 10% fetal bovine serum (FBS) or solutions containing 1 mM glutathione (GSH). Gd was quantified by ICP-MS.

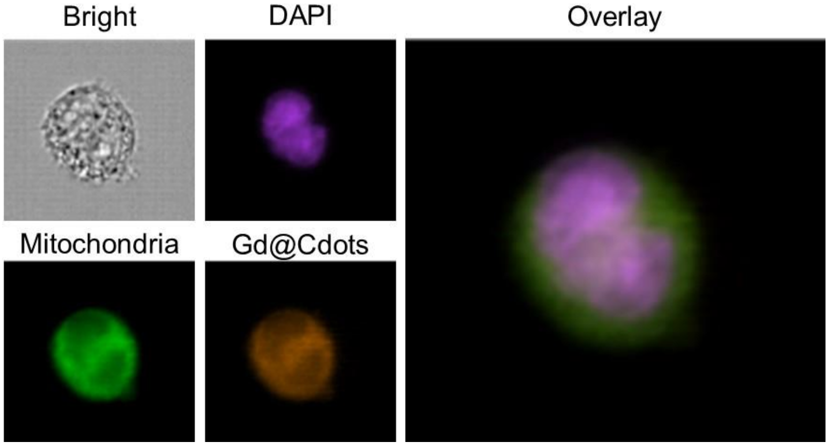

Figure S5. Gd@Cdots accumulation in mitochondria (stained with MitoTracker green). Images were acquired on an ImageStream X Mark II Imaging Flow Cytometer.

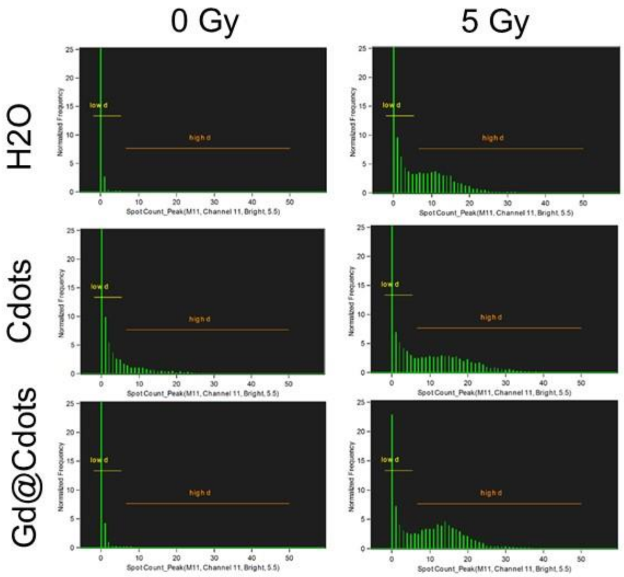

Population	%					
	Control	Cdots	Gd@Cdots	RT	Cdots +RT	Gd@Cdots +RT
DAIP positive rh2aX & cell & focused	100	100	100	100	100	100
low fluorescence & DAIP positive rh2aX & focused	99.7	87.6	99.6	56.1	48.6	42.4
high fluorescence & DAIP positive rh2aX & focused	0.29	10.7	0.39	40.6	48.9	55

Figure S6. Statistics for cell γH2AX loci numbers, evaluated by ImageStream X Mark II Imaging Flow Cytometer.

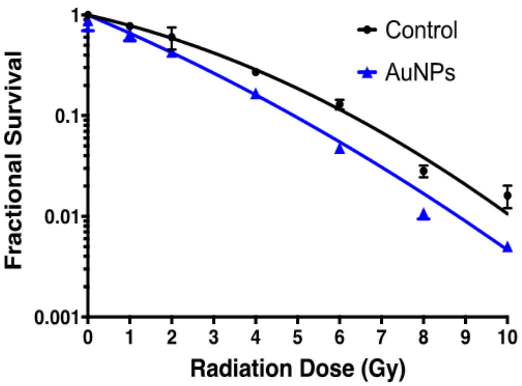

Group	a	b	SF4	REF4
Contro	0.218	0.024	0.285	1.759
AuNPs	0.403	0.013	0.162	

Figure S7. Clonogenic assay with Au nanoparticles (10 µg/mL) and linear-quadratic data fitting.